Ribosomal L12 stalks recruit elongation factors to speed protein synthesis in *Escherichia coli*

Jennifer L. Hofmann,[1] **Theodore S. Yang**,[1] **Alp M. Sunol**,[1] **Roseanna N. Zia**,[3,*]
[1]Department of Chemical Engineering, Stanford University, Stanford, CA 94305
[2]Department of Bioengineering, Stanford University, Stanford, CA 94305
[3]Department of Mechanical and Aerospace Engineering, University of Missouri, Columbia, MO 65211
[*]Correspondence: rzia@missouri.edu

ABSTRACT

Actively translating ribosomes must wait after each elongation step for a new ternary complex (EF-Tu·aa-tRNA·GTP) to be delivered, facilitating rapid codon recognition testing and continued elongation. We recently showed that this wait time rate-limits elongation in *Escherichia coli* due to a competitive combinatoric search through crowded cytoplasm by thousands of *E. coli*'s 42 unique ternary complexes. Here, we investigate whether L12 subunits on ribosomes' surfaces pool translation molecules to reduce this wait time. To do so, we mimic elongation transport and reactions in a physiologically accurate, physics-based model of crowded *E. coli* cytoplasm. We find that L12 pre-loading as much as doubles translation rate by optimizing sampling of novel ternary complexes. But more L12 is not always better: faster-growing bacteria tend to have fewer L12. We resolve this paradox by demonstrating a tradeoff between binding and novel sampling as a function of copy number in *E. coli*. Variable L12 copy numbers may thus have evolved for fast or slow bacterial growth as complementary survival strategies.

INTRODUCTION

All cells must synthesize proteins to grow and divide. In fact, the translation process that produces proteins is the rate-limiting step of bacterial growth [1, 2]. Translation is carried out by the ribosome, which hosts the reaction of multiple translation molecules and initiation, elongation, and termination of protein synthesis. In this work, we examine how the ribosome actively recruits elongation factors to enhance the rate of translation.

The colloidal-scale transport of molecules to the ribosome, along with favorable stoichiometric crowding in the cytoplasm, was recently shown to regulate bacterial elongation rate [3]. In a spatially-resolved physico-chemical model of the *Escherichia coli* cytoplasm (**Fig. 1A**), Maheshwari et al. demonstrated that elongation quickens with growth rate due to optimized encounters between translation molecules. These shorter transport times could not be explained solely via faster kinetics or increasing molecular abundances. Explicit representation of molecular size in the crowded cytoplasm – modeled as systems of polydisperse spheres – was crucial to recover the qualitative speedup in elongation with growth rate (**Fig. 1B**). However, a quantitative gap between *in silico* and bulk experimental measurements remained.

Prediction of the absolute elongation rate requires refined representation of molecular interactions. One such key interaction is between ribosomal stalk proteins and translational GTPases, including elongation factors Tu (EF-Tu) and Ts (EF-Ts) [4–6]. The disordered stalk proteins, called 'L12' in bacteria, exist in multiple copies per ribosome. By binding multiple GTPases simultaneously (**Fig. 2A**), ribosomal stalks are hypothesized to speed translation by increasing the local available concentration of elongation factors [7]. The flexible nature of the stalk had long stymied direct interrogation of its binding dynamics and this 'factor-pooling' hypothesis – that is, until a recent atomic force microscopy study provided direct visualization of archaeal factor binding *in vitro* [8]. Coupled with indirect support from *in vivo* particle tracking experiments [9], these results warrant a closer investigation into the role of the L12 stalk in the physico-chemical regulation of bacterial protein synthesis with growth rate.

Interestingly, L12 is the only protein present in multiple copies, c, per bacterial ribosome. For example, wild-type *E. coli* has four L12 stalks ($c = 4$). Complete or partial removal of the L12 ($c = 0, 2$) greatly reduces EF-Tu binding and slows translation [6]. However, four is not necessarily an 'ideal' L12 copy number. Beyond *E. coli*, bacteria exhibit natural copy numbers between four and eight ($c = 4$-8) [13]. While this variation is well-established, the biological and mechanistic reasons for varying L12 stoichiometry remain a mystery.

Improved *E. coli* translation with L12 copy number ($c = 0, 2, 4$) might seem to imply that even higher natural copy numbers promote more robust growth – or, as previously believed, thermophilicity [14]. However, after surveying and collating findings from the

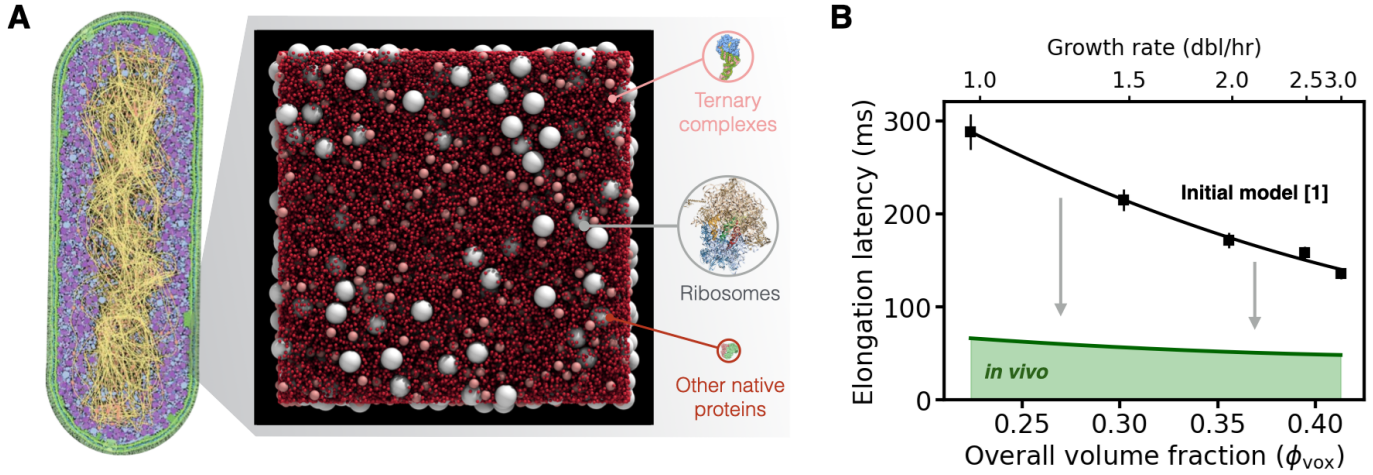

Figure 1: Dynamic simulation of translation elongation in E. coli, including biofidelic attractions between ternary complexes and ribosomes. (A) Visualization of a purely-repulsive isotropic hard sphere E. coli translation voxel at a growth rate of 1 doubling/hour, containing ribosomes (white), EF-Tu·GTP·aa-tRNA ternary complexes (pink), and other native cytoplasmic proteins (red). Protein abundances and volume measurements were compiled from experiments by [3]. Depiction of *E. coli* is adapted with permission from [10]. **(B)** Initial simulations of hard-sphere translation voxels (black symbols, [3]) recovered the qualitative speedup in elongation latency measured in vivo (green line, [11]), but left a quantitative gap (grey arrows).

experimental literature, we found that bacteria with faster growth rates tend to have lower L12 copy numbers (**Fig. 2B**, [12, 13]). To our knowledge, this correlation and apparent paradox has not been previously reported. Thus, we pose a new question: how might factor pooling by L12 in a dense, fast-growing bacterial cytoplasm help explain this puzzle? Moreover, can we deduce a mechanism that couples L12 copy number and bacterial growth rate?

To start, we built on our existing model of *E. coli*, a bacterium well-studied for its adaptability and rapid growth rate [15, 16]. Our recent paper showed that the fastest *E. coli* growth rate (**Fig. 2A**, dashed line) corresponds exactly to an optimization of molecular proximity and mobility in dense cytoplasm [3]. Any further increase in translation molecule density impedes colloidal-scale transport and faster elongation. We hypothesize that a similar tradeoff explains the benefit of lower L12 copy numbers in faster growing bacteria. Factor pooling by L12 stalks increases the local concentration of translation molecules, but might come at the cost of reduced molecular mobility. For *E. coli*, slowed transport from excessive factor pooling would become particularly disadvantageous in dense, fast-growing cytoplasm.

In this work, we expand our existing model of the growth rate dependent *E. coli* cytoplasm (**Fig. 1A**) to incorporate detailed interactions between ribosomal L12 stalks and EF-Tu (**Fig. 2A**). By explicitly modeling the transport dynamics and chemical kinetics of translation elongation, we directly interrogate factor pooling as a function of L12 copy number and cellular growth rate. Our results show that physiological EF-Tu·L12 attractions co-localize the translation machinery while maintaining high molecular mobility. This co-localization reduces wait times at the ribosomal A-site, thereby speeding protein synthesis. We ultimately show that higher L12 copy numbers (c = 6, 8) favor durable ternary complex binding at the expense of rapid combinatoric sampling, offering one explanation for variable L12 stoichiometry. We close with a discussion of broader implications of our work, supporting a colloidal-scale physical basis for cellular fitness.

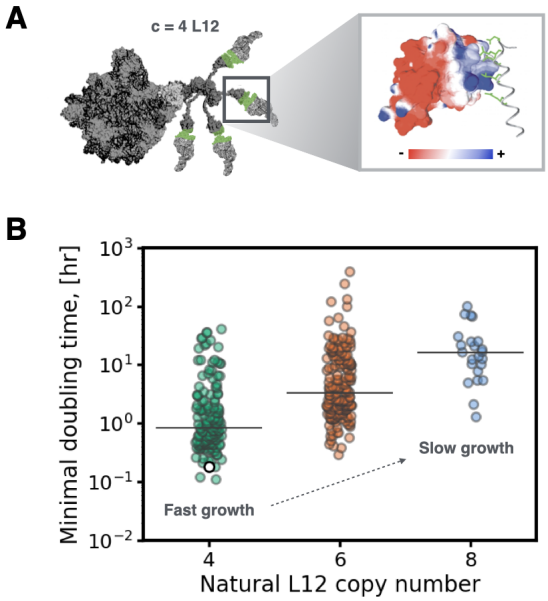

Figure 2: Lower ribosomal L12 copy number correlates with faster bacterial growth. (A) Structural models of ternary complex binding to L12 ribosomal subunits in *E. coli*. (Inset) Contact scheme between the C-terminal domain of a L12 subunit (surface representation on left) and EF-Tu helix D in the ternary complex (ribbon structure on right), adapted with permission from [5]. The surface representation is colored according to charge (red, negative; blue, positive). **(B)** Distributions of minimal doubling times for N = 354 bacteria [12] with known L12 copy numbers (N_4 = 149, N_6 = 182, N_8 = 23, [13]). The line in each plot represents the median value. The fastest observed doubling time of *E. coli* (with *c* = 4 L12) is marked with a white circle. Distributions were compared using the Mann-Whitney U-test ($p < 0.001$ in all cases).

RESULTS

Modeling physiological EF-Tu·L12 interactions recapitulates factor pooling, yet avoids non-specific cytoplasmic aggregation. In our initial model of the *E. coli* cytoplasm, ternary complexes and ribosomes were modeled as isotropic spheres, with entropic forces preventing overlap. Physical contact was accompanied by an aa-tRNA chemical recognition test, followed by ribosome processing using kinetics extracted from a robust literature [3]. These interactions take place simultaneously among thousands of molecules in a densely crowded cytoplasm, where physical size directly sets the rate of molecular diffusion (**Fig. 1A**). A synopsis of the physiological translation voxel model for *E. coli* is provided in ***Methods***.

Here we enhance the surface morphology of the ribosome and the ternary complex to more faithfully represent molecular interactions. We model physiological, limited-valency binding between ribosomal L12 stalks and EF-Tu (**Fig. 2A**) with bumpy surface patches to represent the four L12 per *E. coli* ribosome and one EF-Tu per ternary complex (**Fig. 3A**). These discrete patches – spherical caps of radius 1.2 nm – are endowed with attractions representing the strength and biochemical character of EF-Tu·L12 interactions [5, 17]. We computed this binding site size as the width of the L12 C-terminal domain. Please see ***Methods*** for detailed derivation of these binding parameters. Interaction between any other part of a ternary complex and ribosome is strictly entropic, i.e., hard-sphere repulsion prevents overlap. In reality, ribosomes and ternary complexes are both negatively charged, producing a longer-ranged repulsion. It is straightforward to generalize our model to explore these effects, but is beyond the scope of this study. We consider the potential consequences of this simplification in the ***Discussion*** section. These interactions enable up to four ternary complexes to be bound to each ribosome, potentially speeding aa-tRNA testing via 'factor pooling.' In this next section, we focus on this co-localization and measure occupancy of the L12 sites.

We implemented the limited valency interaction framework described above into dynamic simulations of *E. coli* cytoplasmic voxels. We measured the fraction of ternary complexes bound to ribosomes in our simulation voxels (Eq. 8) to quantify factor pooling (**Fig. 3B**). We found that without ribosomal L12 (*c* = 0), too few ternary complexes are bound relative to *in vivo* data. In the opposite extreme, when attractions fully cover the molecular surfaces, 100% of ternary complexes are bound to ribosomes, an unphysiological result. In contrast, our model with the natural L12 copy number in *E. coli* (*c* = 4) recovers the co-localization measured *in vivo* at 1 dbl/hr [9]. *In vivo* data are available only for this single growth rate, so we extrapolate to higher growth rates by accounting for

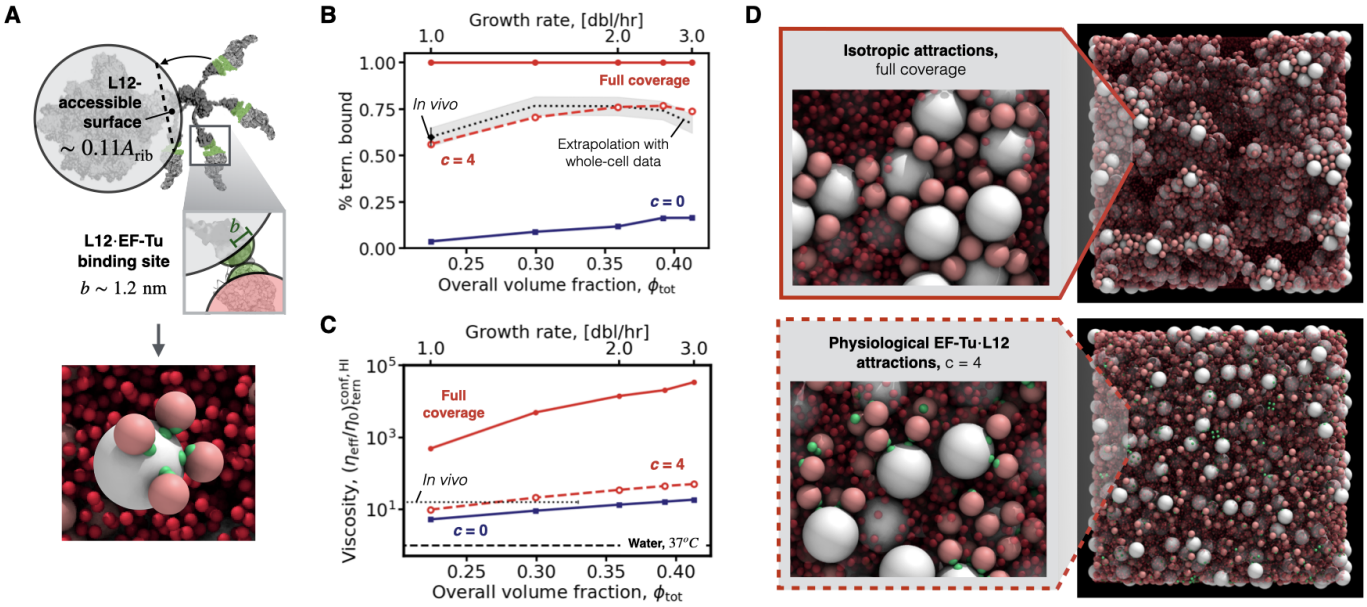

Figure 3: Physiological L12 copy numbers in *E. coli* drives factor pooling, while avoiding non-specific aggregation. (A) Visualization of the physiological, limited-valency model, where attractions between ternary complexes (pink) and ribosomes (white) are restricted to binding sites (green), sized to match that of structural measurements (upper, see Methods). **(B)** The percent of ternary complexes bound to ribosomes (Eq. 8), as a function of growth rate for non-attractive (c = 0, blue solid line), limited-valency (c = 4, red dashed line), and isotropically attractive (full coverage, red solid line) translation voxels. The experimentally-measured value is marked for a growth rate of 1.0 dbl/hr [9], and extrapolated to higher growth rates (dotted black line) as described in ***Supplementary Fig. S1***. **(C)** Effective cytoplasmic viscosity (Eq. 7) experienced by ternary complexes, versus growth rate and volume fraction. The viscosity of water, η_0, at a temperature of 37C (horizontal dashed line) and the estimated *in vivo* viscosity of a protein equal in size to a ternary complex in *E. coli* (horizontal dotted line [18]) are marked. **(D)** Simulation snapshots of the isotropic (top, full coverage) and physiological, limited-valency (bottom, c = 4) models in translation voxels at a growth rate of 3 dbl/hr. The opacity of small crowder proteins is turned down to improve visual clarity (red).

changes in molecular stoichiometry and crowding (***Supplementary Fig. S1***). This extrapolation matches our model's predictions of factor-pooling. Notably, the physiological model (c = 4) captures the non-monotonic trend of the *in vivo* data (***Fig. 3B***). As cell growth speeds up from slow to moderate growth rates, more ternary complexes are bound to ribosomes – an entropic effect dominated by densification of the cytoplasm. Approaching the fastest growth rates, the increase in the abundance of ternary complexes outpaces that of ribosomes [3]. Thus, even if ribosomal binding sites are saturated, there are more 'free' ternary complexes at the fastest growth rates. As a result, even though crowding increases, the changed stoichiometry reduces the relative fraction of ternary complexes bound to ribosomes. The underlying microscopic picture is revealed in ***Supplementary Fig. S2-S3***, where discrete L12 sites drive the mean coordination of ribosomes toward the physiological limit of four bound ternary complexes.

Diffusive mobility – the ability of ternary complexes to diffuse freely – [9] is required for rapid combinatoric testing of aa-tRNAs. We expected factor pooling to affect mobility near the ribosome, because crowding drives up viscosity, which in turn drives down diffusion rates. To study this effect, we calculated the effective viscosity of cytoplasm (**Fig. 3C**), accounting for contributions from hydrodynamics and confinement [19–22] (Eq. 7). As expected, a cytoplasm crowded with mobile ternary complexes (c = 0 L12) is less viscous than a gelled cytoplasm arising from total-coverage attractions ($1/c$ = 0). In contrast, our c = 4 model recovers the *in vivo* viscosity of equivalently-sized proteins in *E. coli* [18] quite well. Physiological L12 copy number thus co-localizes the translation machinery while preserving essential transport dynamics. Simulation snapshots in **Fig. 3D** illustrate the frozen structure in the gelled cytoplasm that causes dynamics to arrest (top) (***Supplementary Fig. S4-S6***) as well as the co-localized, mobile scenario of c = 4 (bottom).

Dynamic co-localization of ternary complexes and ribosomes should be comparable to the duration of the initial aa-tRNA recognition test (lasting from 0.001 to 10 ms [3], see ***Supplementary Fig. S7***), to facilitate immediate loading of a unoccupied A-site. We measured the duration of physical binding events between ternary complexes and ribosomes in our c = 4 L12 model, which revealed two key results (***Supplementary Fig. S8***). First, we found a short-duration peak from t = 0.001 to 0.01 ms driven purely by entropic forces. Second, we found that physiological EF-TU L12 attractions induce transient binding events from t = 0.01 to 1 ms, corresponding to the timescale of the recognition test. These simulation results support a previous inference from *in vivo* particle

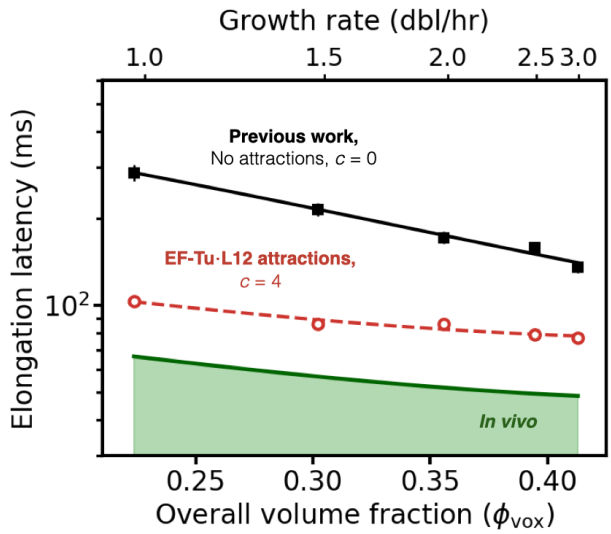

Figure 4: Factor pooling onto ribosomal L12 works alongside stoichiometric crowding to speed elongation. Initial simulations of translation voxels without L12 (c = 0) (black symbols, [3]) recovered the qualitative speedup in elongation latency measured in vivo (green line, [11]). Physiological EF-Tu·L12 interactions (c = 4) drive two- to three-fold shorter elongation latencies (red symbols, dashed line; this work), and improve agreement with experiments. Error bars corresponding to standard error of the mean are on the order of marker size in the c = 4 case.

tracking experiments that ternary complexes can bind to the L12, be tested, and unbind within 2 ms [9].

EF-Tu·L12 interactions facilitate translation by speeding up colloidal-scale transport.

To test how factor pooling impacts elongation latency, we next incorporated intra-ribosomal chemistry into our factor-pooling model. To do so, we incorporated the reaction framework developed by Maheshwari et al. [3]. In simulation, molecules experience physical interactions and undergo chemical reactions that represent the multi-step kinetics leading to peptide bond formation inside the ribosome (see ***Methods***). The primary focus of our first model was the transport and stoichiometry outside the ribosome, in cytoplasm. To fully represent physiological cytoplasm, we accounted for cognate, near-cognate and non-cognate ternary complexes and represented the *in vivo* distribution of relative codon and tRNA abundances over thousands of voxel simulations. A complete explanation of that model and how we used it to measure mRNA elongation latency, can be found in [3].

Elongation latency, τ_{elong}, includes the time a ternary complex spends reacting at the ribosome (reaction latency), diffusing in cytoplasm or pooled around an already-reacting ribosome (combined, transport latency). We discovered that physiological EF-Tu·L12 interactions (c = 4) speed up elongation latency by two- to three-fold compared to our original model without L12 [3] (Fig. 6). This decrease emerges entirely from shortened transport latency (see ***Supplementary Fig. S9***). Mechanistically, EF-Tu·L12 interactions shorten the time ribosomes must wait for a matching ternary complex. Whereas our first model predicted the qualitative speed-up with growth rate, the current refined model improves quantitative agreement compared with *in vivo* measurements [11]. This improved prediction of absolute elongation rate supports the mechanistic picture advanced here and our hypothesis that factor pooling speeds translation by 'pre-loading' the ribosome with ternary complexes.

L12 copy number: optimizing binding and sampling in *E. coli* cytoplasm supports fast growth

Finally, we asked how having varied L12 copy numbers, $c = 2, 4, 6, 8$, might impact translation elongation in E. coli. We built ribosome models with two, six, and eight L12 binding sites, corresponding to the case when one L12 dimer is knocked out in *E. coli* ($c = 2$) [23] and physiological stoichiometries in other bacteria ($c = 6, 8$, see **Fig. 2B**) [13]. In simulations of translation voxels at 3 dbl/hr, we found that binding events between ternary complexes and ribosomes last up to milliseconds when copy number $c \geq 4$, (green shaded region, **Fig. 5A**). These results indicate that higher copy numbers are sufficient to pre-load ternary complexes and reduce ribosomal wait times, as observed earlier for the $c = 4$ case. The knock-out case, $c = 2$, dramatically reduces encounter durations, indicating that binding times with two L12 stalks are well below those required for effective factor pooling, consistent with prior experimental measurements [23].

But more is not always better. Durable co-localization can come at the cost of rapid combinatoric sampling of new ternary com-

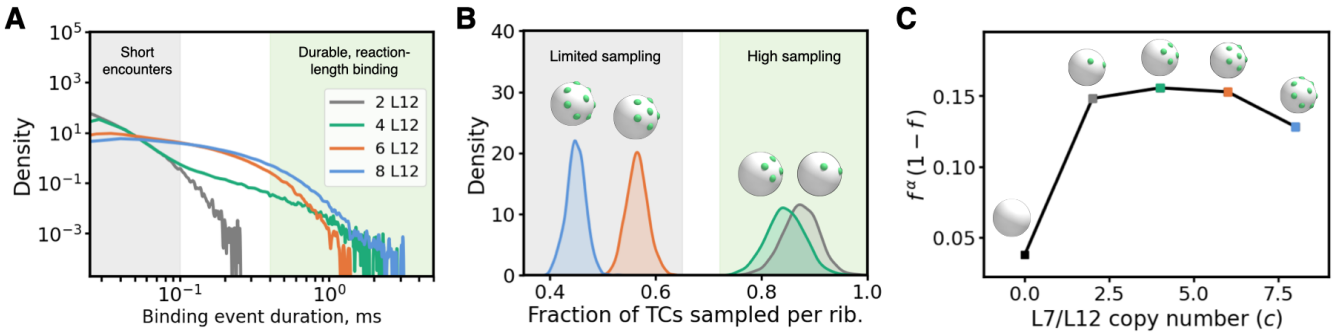

Figure 5: Physiological L12 stoichiometry optimizes ternary complex binding and sampling at the fastest *E. coli* growth rate. (A) Probability density function (shown as the kernel density estimate, KDE) of the duration of binding events for simulations with L12 copy numbers c = 2-8. Binding occurs when surface-to-surface distance between ternary complex and ribosome ≤ 2.1 nm. Green background highlights binding events of duration comparable to duration of initial aa-tRNA recognition test. Grey background highlights encounters too short for the recognition test to take place. **(B)** Fraction of ternary complex population sampled by each ribosome for four L12 copy numbers. Legend same as (A). **(C)** The tradeoff between bound and freely searching ternary complexes in *E. coli* translation voxels at growth rate 3 dbl/hr, as a function of L12 copy number c. Here, f is the fraction of ribosome-bound TCs and $\alpha = 1.71$ is the ratio of Boltzmann state energies that produces $f^{in\ vivo}$ (see Methods).

plexes (**Fig. 5B**). We simulated translation elongation in voxels for $c = 2, 4, 6, 8$ and monitored how many unique ternary complexes, out of the entire pool, were sampled by each ribosome. High values indicate that a ribosome has many unique encounters with ternary complexes, increasing its chances for cognate interactions. As expected, the knockout case maintains the highest sampling, 87% – but encounters are over before recognition testing can begin. And although $c = 6$ and 8 encounters are more durable, the ribosomes sample only 55% and 45% of the combinatoric space, respectively (**Fig. 5B**). In the physiological $c = 4$ case, ribosomes are still able to sample 85% of ternary complexes on average, while also facilitating many long-duration binding events. Overall, there is a key tradeoff between durable binding and broad sampling.

We quantify this tradeoff as the product of the probabilities of the bound and freely mobile ternary complex states (Fig. 5A-B), plotted in **Fig. 5C**. Beyond the physiological copy number of four L12 per ribosome, we found that the benefits of co-localization (shorter ribosomal wait times) are wiped out by the deleterious effects of limiting ternary complex mobility (less sampling of new ribosomes) at the densest, fastest *E. coli* growth rate. That is, $c = 4$ is the optimal copy number in our simulations, as well as in live *E. coli*. In the ***Discussion***, we speculate about how a copy number of four L12 might have evolved to maximize this tradeoff and support faster growth rates more broadly.

DISCUSSION

The speed-up in elongation rate as *E. coli* growth quickens originates from a physical mechanism by which advantageous molecular stoichiometry is brought into closer proximity [3]. This 'stoichiometric crowding' effect optimizes encounters between cognate translation molecules, shortening the diffusive search time of ternary complexes to ribosomes. However, an approximately three-fold gap between predicted and measured absolute elongation latencies [11] suggested additional mechanisms might further speed elongation by facilitating this searching and binding process.

L12 subunits have been hypothesized to pool translation factors, including EF-Tu in ternary complexes, near ribosomes [4–7, 17, 24]. This advantageous co-localization could further shorten the time a ribosome must wait to test a new aa-tRNA. To explore this idea, we built a dynamic computational model that efficiently incorporated attractions between ternary complexes and ribosomes in voxels of the growth-rate dependent *E. coli* cytoplasm. Our model enabled interrogation of transient binding dynamics at higher resolution than currently accessible by particle tracking methods [9]. We applied our model to mechanistically connect microscopic interaction details to bulk cellular behaviors, i.e., elongation rate.

We first found that physiological EF-Tu·L12 attractions drive durable co-localization of the translation machinery over timescales comparable to the aa-tRNA recognition test, while maintaining a mobile cytoplasm. Next, we showed with direct measurements that L12 subunits play a central role in setting the rate of protein synthesis by pooling ternary complexes near the ribosome, and doubling the elongation rate. This finding demonstrates a cooperation between attractions and stoichiometric crowding that improves per-ribosome productivity. Our results provide further support to the discovery that stoichiometric crowding speeds protein

synthesis in faster-growing *E. coli*. Moreover, the absolute rate of elongation is modulated by factor pooling onto ribosomal L12. Beyond EF-Tu, our findings also have implications for other L12-mediated interactions, including with the recently identified CRISPR-Cas-associated protein Cami1 [25].

The remaining quantitative gap between predicted and measured absolute elongation rate could be explained by additional physicochemical mechanisms, including attractions between mRNA codons and tRNA anticodons [26] that could 'pre-sort' cognate ternary complexes near ribosomes. Modest discrepancies between the *in vitro* chemical kinetic parameters used in our model and real *in vivo* rates – arising, for example, from differences in solvent conditions – could also close the gap [3]. Future work might further refine physical interaction details to include representation of surface roughness, repulsions between negatively charged tRNA and rRNA, or the mobility of the L12 arms. We note that experimental data for dynamics and co-localization are limited to a single growth rate in our studied range [9]. *In vivo* data at faster *E. coli* growth rates would enable further validation of crowding-dependent behaviors in our model.

By assessing literature data for copy numbers across bacterial species, we revealed that faster growing bacteria tend to have fewer L12 – seeming to contradict the factor pooling hypothesis [7]. To resolve this paradox, we demonstrated a putative mechanism underlying the optimal L12 stoichiometry in *E. coli*. The physiological *E. coli* L12 copy number maximizes durable binding and frequent sampling of new ternary complexes in dense, fast-growing cytoplasm. Higher copy numbers of six and eight L12 favor binding over sampling. This result appears to demonstrate an evolutionary pressure to optimize the tradeoff between combinatoric sampling and simply binding.

Given the hypothesis that the last bacterial common ancestor had six L12 [13], we speculate that copy numbers of c = 4 and c = 8 could have emerged to support faster and slower growth, respectively. For example, a copy number of four L12 could have evolved to optimize sampling and binding of ternary complexes under crowded conditions – that is, if the densification of cytoplasm with growth rate is a general feature of bacteria. Faster and slower growth strategies permit other survival mechanisms such as dormancy to dominate [27]. We note that cyanobacteria such as *Trichodesmium erythraeum* and *Gloeobacter violaceus* make up the majority of bacteria with eight L12, suggesting unique evolutionary pressure that favors a cytolasmic environment with enhanced binding over sampling. We encourage further work to explore the implications of this hypothesis in experiment – e.g., how L12 copy number might be engineered in bacteria to tune maximum or minimum growth rate.

MATERIALS AND METHODS

Computational Model

We constructed computational representations of 'translation voxels' of the *E. coli* cytoplasm (**Fig. 1A**) in the molecular dynamics package LAMMPS [28], following the initial model described in [3]. In this work, each periodically-replicated voxel contains approximately 200,000 nearly-hard colloidal spheres representing ribosomes (with radius $a_{\mathrm{rib}} = 13\,\mathrm{nm}$), ternary complexes ($a_{\mathrm{tern}} = 5.9\,\mathrm{nm}$), and other native cytoplasmic proteins ($a_{\mathrm{prot}} = 2\,\mathrm{nm}$). The abundance of each molecule (N_i), voxel length (l_{vox}), and total voxel volume fraction (ϕ_{tot}) depend on cellular growth rate (see ***Supplementary Table S1***). Please see [3] for a detailed description of how voxel parameters were obtained from experimental measurements.

A pair of molecules i and j can interact in translation voxels via entropic or attractive components, defined by the potential:

$$\frac{V\left(r_{ij}\right)}{k_{\mathrm{B}}T} = \begin{cases} V_{\mathrm{rep}} = 6\left(1 - e^{-60\left(r_{ij}-\sigma_{ij}\right)}\right)^2 - \varepsilon_{ij} & \text{if } r_{ij} \leq \sigma_{ij} \\ V_{\mathrm{attr}} = -\varepsilon_{ij}\sigma_{ij}/r_{ij}e^{-z\left(r_{ij}/\sigma_{ij}-1\right)} & \text{if } r_{ij} > \sigma_{ij}, \end{cases} \tag{1}$$

where r_{ij} is the magnitude of the unit vector $\hat{\boldsymbol{r}}_{ij}$ pointing from the center of particle j to the center of particle i, k_{B} is the Boltzmann constant, and T is the absolute temperature. Entropic exclusion is enforced via a Morse potential, V_{rep}, previously demonstrated to recover hard-sphere behavior [29]. The hard-sphere contact distance σ_{ij} is defined as the sum of particle radii, a_i and a_j.

Previous structural homology-based and kinetic experiments suggest that the EF-Tu·L7/L12 interaction consists of a hydrophobic patch flanked by two salt bridges [5, 17]. To capture the exponential character of such interactions [30, 31], we represented the at-

traction between ternary complexes and ribosomes via a Yukawa potential, V_{attr}. The attraction range of hydrophobic interactions and salt bridges (approximately $0.4\,\mathrm{nm}$ [31, 32]) corresponds with a decay rate constant $z = 10/\sigma_{ij}$ in Eq. 1. The characteristic attraction strength, ε_{ij}, sets the depth of the potential well. We estimated the *in vivo* attraction strength to be $\varepsilon_{\mathrm{t,r}}^{\mathrm{exp}} = 16\,k_{\mathrm{B}}T$, assuming each salt bridge contributes $3\,\mathrm{kcal/mol}$ ($4.9\,k_{\mathrm{B}}T$ at 37^oC, [33]) and the hydrophobic patch contributes $4\,\mathrm{kcal/mol}$ ($6.5\,k_{\mathrm{B}}T$ at 37^oC). To calculate the hydrophobic contribution, we assumed that a $18\,\mathrm{cal\,mol^{-1-2}}$ free energy density [34] is distributed over a hemisphere of diameter 11.8, the size of the hydrophobic region of the L7/L12 C-terminal domain (PDB code ICTF [35]). We also investigated weaker isotropic attraction strengths of $\varepsilon_{\mathrm{t,r}} = 3\,k_{\mathrm{B}}T$ and $6\,k_{\mathrm{B}}T$, which have been demonstrated to drive formation of phase-separated droplets [36] and arrested gel networks [37], respectively. Interactions between other types of molecules are purely repulsive at contact and otherwise do not interact, i.e., $\varepsilon_{ij\neq\mathrm{t,r}} = 0$.

To build a limited-valency interaction model, we first calculated the ribosome surface area accessible to the highly mobile L7/L12 subunits. Using the structural model from [6], we projected the range of movement of all four L7/L12 subunits onto a ribosome body of size $a_{\mathrm{rib}} = 13\,\mathrm{nm}$ (**Fig. 3A**). The resulting spherical cap with base radius $h = 0.61\,a_{\mathrm{rib}}$ has a surface area $A_{\mathrm{cap}} = 220.4\,\mathrm{nm}^2$, approximately 11% of the total ribosome surface area $A_{\mathrm{rib}} = 2123.7\,\mathrm{nm}^2$. We embedded four spheres representing the L7/L12 subunits at evenly spaced intervals around the boundary of this accessible surface area. These spheres were inset to expose small binding site caps with base radii $b = 1.2\,\mathrm{nm}$, the measured size of the L7/L12 C-terminal domain (PDB code *ICTF* [35]). All measurements of structural models in this work were conducted using UCSF ChimeraX [38]. We embedded an identical inset sphere in the surface of each ternary complex to represent the equivalent binding site on EF-Tu (**Fig. 3A**). In the limited-valency model, the Yukawa attraction V_{attr} (Eq. 1) is only felt between these inset binding sites representing the EF-Tu and L7/L12 domains.

To interrogate a range of L7/L12 copy numbers, c, we modeled ribosomes with two, six, and eight binding sites of identical size to the previously described $c = 4$ model. For $c = 2$, we inset the binding sites on opposite sides of the L7/L12 accessible surface area (**Fig. 5A, 7**). For $c = 6$ and $c = 8$, we inset one binding site at the center and five and seven binding sites, respectively, equally spaced around the circumference of the L7/L12 accessible surface area. When $c \geq 6$, we expanded the accessible surface area to maintain the same binding site spacing as in the $c = 4$ case to prevent a single ternary complex from binding to multiple L7/L12 at a time.

Dynamic Simulation Method

Molecules are immersed in an implicit Newtonian solvent with viscosity $\eta = 0.6913\,\mathrm{mPa/s}$ and density $\rho = 0.99336\,\mathrm{g/cm^3}$, chosen to represent water at 37° C. The small size of translation molecules sets a vanishingly small Reynolds number, $Re = \rho U a_i/\eta$, where U is the characteristic particle velocity. Fluid motion is thus governed by Stokes' equations, whereas particle motion is governed by the Langevin equation [39]:

$$\boldsymbol{m} \cdot \frac{d\boldsymbol{U}}{dt} = \boldsymbol{F}^{\mathrm{H}} + \boldsymbol{F}^{\mathrm{B}} + \boldsymbol{F}^{\mathrm{P}}, \tag{2}$$

where $\boldsymbol{m}$ is the mass tensor and $\boldsymbol{U}$ is the particle velocity. $\boldsymbol{F}^{\mathrm{H}}$ is the hydrodynamic force on each particle i given by Stokes drag law $\boldsymbol{F}_i^{\mathrm{H}} = -6\pi\eta a_i\,[\boldsymbol{U}_i - \langle\boldsymbol{u}\rangle]$, where $\langle\boldsymbol{u}\rangle$ is the bulk fluid velocity, which is zero for a quiescent prokaryotic cytoplasm. The stochastic Brownian force $\boldsymbol{F}^{\mathrm{B}}$ emerges from thermal solvent fluctuations and obeys Gaussian statistics:

$$\boldsymbol{F}_i^{\mathrm{B}} = 0,\ \overline{\boldsymbol{F}_i^{\mathrm{B}}(0)\boldsymbol{F}_i^{\mathrm{B}}(t)} = 2k_{\mathrm{B}}T(6\pi\eta a_i)\boldsymbol{I}\delta(t), \tag{3}$$

where overbars indicate averages over long times compared to the solvent timescale, $\boldsymbol{I}$ is the identity tensor, and $\delta(t)$ is the Dirac delta function. The deterministic interparticle force $\boldsymbol{F}^{\mathrm{P}}$ is the gradient of the interaction potential V_{ij} between a particle pair (Eq. 1):

$$\boldsymbol{F}_i^{\mathrm{P}} = -\sum_j \frac{\partial V_{ij}(r_{ij})}{\partial r_{ij}}\hat{\boldsymbol{r}}_{ij}. \tag{4}$$

We instantiated the initial distribution of finite sized molecules in translation voxels using PACKMOL [40]. In LAMMPS, Eq. 2 is integrated forward in time using the velocity-Verlet method [41] and a Langevin thermostat [42] to solve for particle trajectories. We chose a sufficiently small discretization timestep, $\Delta t = 13\,\mathrm{ps}$, and damping factor, $d = 0.01$, to recover the inertia-less physics of the

Stokes flow regime [29]. In the limited-valency model, each ribosome and ternary complex with inset binding sites is treated as a rigid body using the 'fix rigid' command in LAMMPS. Simulations were evolved for $1.3\,\mathrm{ms}$, with full particle trajectories output every $130\,\mathrm{ns}$. Visualizations of simulations were created using Visual Molecular Dynamics (VMD, [43]).

Dynamics and Rheology

We monitored dynamics by tracking particle positions throughout simulation and computing their mean-square displacement (MSD) over time

$$\mathrm{MSD}_i = \langle \Delta \boldsymbol{x}_i \Delta \boldsymbol{x}_i \rangle, \tag{5}$$

where $\Delta \boldsymbol{x} = \boldsymbol{x}(t) - \boldsymbol{x}(0)$ is the change in particle position from the initial time to the current time t, and i is the particular molecular species (ribosome, ternary complex, or small native protein). Please see ***Supplementary Fig. S10-S11***. Angle brackets denote an ensemble average over all molecules of that species. We extracted the long-time self-diffusivity, $D^s_{\infty,i}$ for each species from the slope of the MSD over long times

$$D^s_{\infty,i} = \frac{1}{6} \frac{d\,(\mathrm{MSD}_i)}{dt}\bigg|_{t=0.4-0.6\,\mathrm{ms}}. \tag{6}$$

Cellular confinement and the presence of hydrodynamic interactions are expected to slow diffusion *in vivo*. Thus, to compare dynamics in our freely-draining, unconfined model to experimental measurements, we scaled $D^s_{\infty,i}$ by a volume fraction dependent factor which accounts for both confinement and hydrodynamic effects. We derived this scaling factor using analytical theory [44, 45] and results from confined Brownian and Stokesian Dynamics simulations [20, 22]. Details can be found in the ***Supplementary Information, Fig. S12***.

We used this molecular diffusivity to calculate the effective cytoplasmic viscosity experienced by ternary complexes $\eta_{\mathrm{eff,tern}}$, given by the Stokes-Einstein relation [46, 47], which is a reasonable approximation in concentrated suspensions if the produced viscosity is interpreted as a microscopic rather than a bulk viscosity [48]:

$$\eta_{\mathrm{eff,tern}} = \frac{k_{\mathrm{B}}T}{6\pi a_{\mathrm{tern}} D^s_{\infty,\mathrm{tern}}}, \tag{7}$$

Here, $D^s_{\infty,\mathrm{tern}}$ is the scaled long-time self-diffusivity, accounting for hydrodynamic and confinement effects (***Supplementary Fig. S12***). We normalized this effective viscosity by that of water at $37^o\,C$, $\eta_0 = 0.6913\,\mathrm{cP}$, to capture the entropic contribution due to finite molecular size.

Binding Metrics

To quantify co-localization of the translation machinery, we calculated the fraction of ribosome-bound ternary complexes, f, in each voxel:

$$f = \frac{N_{\mathrm{tern,bound}}}{N_{\mathrm{tern,tot}}} \tag{8}$$

where $N_{\mathrm{tern,tot}}$ is the total number and $N_{\mathrm{tern,bound}}$ is the ribosome-bound number of ternary complexes. A ternary complex, i, is considered bound to a ribosome, j, if their center-to-center separation r_{ij} is less than the maximum bond distance $r_{\mathrm{cut}} = 21\,\mathrm{nm}$ (for details, see ***Supplementary Fig. S8A***). This bound fraction was estimated *in vivo* by Mustafi and Weisshaar to be $f_{\mathrm{exp}} = 0.6$ at a growth rate of 1 dbl/hr [9]. In ***Supplementary Fig. S1***, we describe how we extrapolated this experimental measurement to higher growth rates by accounting for changes in molecular stoichiometry and crowding.

Binding Times and Sampling Rates

We quantified the duration of individual binding events by computing the time that ternary complexes spend within the maximum bond distance r_{cut} of a ribosome. According to this binding definition, we tracked the state of each ternary complex as 'bound' or 'unbound' over the $1.3\,\mathrm{ms}$ simulation evolution. If a ternary complex departed a bound state, the duration of that event was recorded in the distribution of binding times. The identity of that ternary complex was also recorded as having been 'sampled' by that ribosome. At the end of the analysis window, we computed the number of unique ternary complexes that each ribosome sampled, normalized by the maximum number sampled in the $c = 2$ case. We visualized the probability distributions of binding event durations

and sampling fractions using the Python Seaborn package for kernel density estimates.

We quantified the tradeoff between co-localization and mobility by the product of the fractions of bound, f, and freely diffusing ternary complexes, $(1-f)$. Without scaling, this product would be maximized at $f = 0.5$, whereas $f^{\textit{in vivo}} = 0.67$ at a growth rate of 3 dbl/hr (**Fig. 5C**). To account for this favoring of the bound state *in vivo*, we raised the bound fraction f to a power $\alpha = 1.71$, corresponding to the difference in energies $(\varepsilon_{\text{free}} - \varepsilon_{\text{bound}})$ in a two-state Boltzmann distribution [49]:

$$\frac{p_{\text{bound}}}{p_{\text{free}}} = e^{\varepsilon_{\text{free}} - \varepsilon_{\text{bound}}} \tag{9}$$

where $p_{\text{bound}} = f^{\textit{in vivo}}$ and $p_{\text{free}} = 1 - f^{\textit{in vivo}}$.

Modeling Chemical Reactions and Elongation Latencies

To simulate the coupled physics and chemistry of translation elongation, we developed a bespoke version of LAMMPS [28] that allows for changes to interparticle interactions based on distance, time, and particle type. In each translation voxel simulation ($N_{\text{sim}} = 1,170$ per growth rate), we randomly picked a ribosome to track and classified all ternary complexes as either cognates or non-cognates based on the physiological distribution of codon and tRNA abundances, following the framework developed in [3]. To represent codon-anticodon testing, we modified our limited-valency interaction model to include internal sites within each ribosome and ternary complex, representing the A-site codon and tRNA anti-codon, respectively (see ***Supplementary Fig. S13***).

In simulation, we allowed particles to diffuse and interact as in the physics-only model described above. To simulate the initial aa-tRNA recognition test, we used a distance-based rule to change the pairwise interactions between ribosomes and ternary complexes that are in close physical proximity. Namely, if the center-to-center distance between L7/L12 and EF-Tu sites is less than 1.05 times their hard-sphere contact distance (i.e., $2.52\,\text{nm}$), we considered their respective ribosome and ternary complex as having begun reacting. We note that molecules can only be involved in one reaction at a time. To simulate the entry of a captured ternary complex into the ribosome, we turned off the hard sphere repulsion between reacting pairs, and turn on a $16\,k_{\text{B}}T$ attraction between their internal A-site codons and tRNA anti-codons (see ***Supplementary Fig. S13***). The duration of each reaction was drawn from a latency distribution derived from experimental kinetic rates [3], depending on if the codon and anticodon are cognates or non-cognates (see ***Supplementary Fig. S7***). We accounted for the presence of near-cognate ternary complexes by randomly scaling non-cognate reaction durations by 3.3-fold with a 20% probability, as in [3]. If the reaction is not successful, the simulation was allowed to proceed for the sampled reaction duration, before ternary complex release was imposed by a soft repulsion between the reacting pair. Once the center-to-center distance is above a distance threshold ($12.2\,\text{nm}$), both particles in the simulation are returned to the non-reacting pool and can start another reaction upon their next encounter. When a successful cognate match is found, the simulation is terminated.

The previous reaction framework [3] scaled physiological kinetic rates by 600-fold, which enabled computational tractability while maintaining a well-mixed distribution of particles within simulation. Since physical binding events in our limited-valency model last ten times longer on average than in non-attractive voxels, we scaled kinetic rates here by only 60-fold. See a detailed discussion of this speedup in [3], particularly the section "Acceleration of translation voxel simulations to reduce run time and cost."

For each growth rate, we calculated a reaction latency ($\overline{\tau}_{\text{rxn}}$), defined as the time the cognate ternary complex spends in reactions; an elongation latency ($\overline{\tau}_{\text{elong}}$), defined as the total time the matching ribosome spends unbound or in reactions; and a transport latency ($\overline{\tau}_{\text{transport}}$), calculated as the difference between the elongation and reaction latency. We followed the method described in detail in [3], including the impacts of physiological variability in cognate abundances.

Prokaryotic L7/L12 Copy Number

L7/L12 copy number, c, has been quantified for more than $1,200$ bacteria, mitochondria, and chloroplasts by computational analysis and mass spectrometry [13]. We focused on a subset of $N = 354$ bacteria across five phyla for which minimal doubling times are also known (Table S2), gathered from the '$\text{condensed_traits_NCBI.csv}$' supplementary file of [50] (`https://doi.org/10.6084/m9.figshare.12221732`). We separated this subset into three populations of size N_c according to L7/L12 copy number, where $N_4 = 149$,

$N_6 = 182$, and $N_8 = 23$. We then visualized the probability distribution of minimal doubling times for each population using the Python Seaborn package for kernel density estimates. We compared the means of the distributions via the Mann-Whitney U-test in SciPy, with $p < 0.001$ for all cases.

ACKNOWLEDGMENTS

The authors thank Drew Endy, Akshay Maheshwari, and Emma Gonzalez for many fruitful discussions and insights regarding the translation voxel model. This work was supported by the National Science Foundation Graduate Research Fellowships under Grant No. 1656518 for J.L.H. and A.M.S., Stanford Graduate Fellowships for A.M.S and T.S.Y., and an ARCS Foundation Award for J.L.H..

Computing was performed on the Sherlock cluster at the Stanford Research Computing Center (SRCC) and on Stampede2 at the Texas Advanced Computing Center (TACC). SRCC resources were provided by Stanford University, while resources at TACC were supported by the National Science Foundation's Extreme Science and Engineering Discovery Environment (XSEDE) Research Award No. CTS130035 and Advanced Cyberinfrastructure Coordination Ecosystem: Services & Support (ACCESS) Research Award No. CHM230007.

AUTHOR CONTRIBUTIONS

J.L.H. and R.N.Z. designed research; J.L.H. and T.S.Y. performed research; J.L.H., T.S.Y., and A.M.S. analyzed data; and J.L.H., T.S.Y., A.M.S., and R.N.Z. wrote the paper.

AUTHOR COMPETING INTERESTS

The authors declare no competing interests

REFERENCES

[1] Ken A. Dill, Kingshuk Ghosh, and Jeremy D. Schmit. Physical limits of cells and proteomes. *Proceedings of the National Academy of Sciences of the United States of America*, 108:17876–17882, 11 2011.

[2] Nathan M. Belliveau, Griffin Chure, Christina L. Hueschen, Hernan G. Garcia, Jane Kondev, Daniel S. Fisher, Julie A. Theriot, and Rob Phillips. Fundamental limits on the rate of bacterial growth and their influence on proteomic composition. *Cell Systems*, 12:924–944.e2, 9 2021.

[3] Akshay J. Maheshwari, Alp M. Sunol, Emma Gonzalez, Drew Endy, and Roseanna N. Zia. Colloidal physics modeling reveals how per-ribosome productivity increases with growth rate in escherichia coli. *mBio*, 12 2022.

[4] Holger Stark, Marina V. Rodnina, Jutta Rinke-Appel, Richard Brimacombe, Wolfgang Wintermeyer, and Marin Van Heel. Visualization of elongation factor tu on the escherichia coli ribosome. *Nature 1997 389:6649*, 389:403–406, 1997.

[5] Ute Kothe, Hans Joachim Wieden, Dagmar Mohr, and Marina V. Rodnina. Interaction of helix d of elongation factor tu with helices 4 and 5 of protein l7/12 on the ribosome. *Journal of Molecular Biology*, 2004.

[6] Mihaela Diaconu, Ute Kothe, Frank Schlünzen, Niels Fischer, Jörg M. Harms, Alexander G. Tonevitsky, Holger Stark, Marina V. Rodnina, and Markus C. Wahl. Structural basis for the function of the ribosomal l7/12 stalk in factor binding and gtpase activation. *Cell*, 2005.

[7] Anders Liljas and Suparna Sanyal. The enigmatic ribosomal stalk. *Quarterly reviews of biophysics*, 51:e12, 2018.

[8] Hirotatsu Imai, Toshio Uchiumi, and Noriyuki Kodera. Direct visualization of translational gtpase factor pool formed around the archaeal ribosomal p-stalk by high-speed afm. *Proceedings of the National Academy of Sciences*, 117(51):32386–32394, 2020.

[9] Mainak Mustafi and James C. Weisshaar. Simultaneous binding of multiple ef-tu copies to translating ribosomes in live escherichia coli. *mBio*, 9, 1 2018.

[10] D.S. Goodsell. Elongation factors. *RCSB Protein Data Bank*, 9 2006.

[11] Hans Bremer and Patrick P. Dennis. Modulation of chemical composition and other parameters of the cell at different exponential growth rates. *EcoSal Plus*, 3, 2 2008.

[12] Jake L. Weissman, Shengwei Hou, and Jed A. Fuhrman. Estimating maximal microbial growth rates from cultures, metagenomes, and single cells via codon usage patterns. *Proc. Natl. Acad. Sci. U. S. A.*, 118(12), mar 2021.

[13] Iakov I. Davydov, Ingo Wohlgemuth, Irena I. Artamonova, Henning Urlaub, Alexander G. Tonevitsky, and Marina V. Rodnina. Evolution of the protein stoichiometry in the L12 stalk of bacterial and organellar ribosomes. *Nat. Commun.*, 4, 2013.

[14] Yasushi Maki, Tetsuo Hashimoto, Min Zhou, Takao Naganuma, Jun Ohta, Takaomi Nomura, Carol V Robinson, and Toshio Uchiumi. Three binding sites for stalk protein dimers are generally present in ribosomes from archaeal organism. *Journal of biological chemistry*, 282(45):32827–32833, 2007.

[15] Mingzhu Liu, Tim Durfee, Julio E Cabrera, Kai Zhao, Ding J Jin, and Frederick R Blattner. Global transcriptional programs reveal a carbon source foraging strategy by escherichia coli*. *Journal of Biological Chemistry*, 280(16):15921–15927, 2005.

[16] Zachary D Blount. The unexhausted potential of e. coli. *elife*, 4:e05826, 2015.

[17] Hans Joachim Wieden, Wolfgang Wintermeyer, and Marina V. Rodnina. A common structural motif in elongation factor ts and ribosomal protein l7/12 may be involved in the interaction with elongation factor tu. *Journal of Molecular Evolution 2001 52:2*, 52:129–136, 2001.

[18] Wojciech M. Smigiel, Luca Mantovanelli, Dmitrii S. Linnik, Michiel Punter, Jakob Silberberg, Limin Xiang, Ke Xu, and Bert Poolman. Protein diffusion in escherichia coli cytoplasm scales with the mass ofthe complexes and is location dependent. *Science Advances*, 8:5387, 8 2022.

[19] G. K. Batchelor. Brownian diffusion of particles with hydrodynamic interaction. *J. Fluid Mech.*, 74(1):1–29, mar 1976.

[20] Christian Aponte-Rivera, Yu Su, and Roseanna N. Zia. Equilibrium structure and diffusion in concentrated hydrodynamically interacting suspensions confined by a spherical cavity. *Journal of Fluid Mechanics*, 836:413–450, 2 2018.

[21] Emma Gonzalez, Christian Aponte-Rivera, and Roseanna N. Zia. Impact of polydispersity and confinement on diffusion in hydrodynamically interacting colloidal suspensions. *J. Fluid Mech.*, 925:35, 2021.

[22] Alp M. Sunol and Roseanna N. Zia. Confined Brownian suspensions: Equilibrium diffusion, thermodynamics, and rheology. *J. Rheol. (N. Y. N. Y).*, 67(2):433, jan 2023.

[23] Chandra Sekhar Mandava, Kristin Peisker, Josefine Ederth, Ranjeet Kumar, Xueliang Ge, Witold Szaflarski, and Suparna Sanyal. Bacterial ribosome requires multiple L12 dimers for efficient initiation and elongation of protein synthesis involving IF2 and EF-G. *Nucleic Acids Res.*, 40(5):2054–2064, mar 2012.

[24] Rebecca M. Voorhees and V. Ramakrishnan. Structural basis of the translational elongation cycle. *https://doi.org/10.1146/annurev-biochem-113009-092313*, 82:203–236, 6 2013.

[25] Irmantas Mogila, Giedre Tamulaitiene, Konstanty Keda, Albertas Timinskas, Audrone Ruksenaite, Giedrius Sasnauskas, Česlovas Venclovas, Virginijus Siksnys, and Gintautas Tamulaitis. Ribosomal stalk-captured carf-rele ribonuclease inhibits translation following crispr signaling. *Science*, 382(6674):1036–1041, 2023.

[26] H. J. Grosjean, S. De Henau, and D. M. Crothers. On the physical basis for ambiguity in genetic coding interactions. *Proc. Natl. Acad. Sci.*, 75(2):610–614, feb 1978.

[27] Declan A Gray, Gaurav Dugar, Pamela Gamba, Henrik Strahl, Martijs J Jonker, and Leendert W Hamoen. Extreme slow growth as alternative strategy to survive deep starvation in bacteria. *Nature communications*, 10(1):890, 2019.

[28] Aidan P. Thompson, H. Metin Aktulga, Richard Berger, Dan S. Bolintineanu, W. Michael Brown, Paul S. Crozier, Pieter J. in 't Veld, Axel Kohlmeyer, Stan G. Moore, Trung Dac Nguyen, Ray Shan, Mark J. Stevens, Julien Tranchida, Christian Trott, and Steven J. Plimpton. Lammps - a flexible simulation tool for particle-based materials modeling at the atomic, meso, and continuum scales. *Computer Physics Communications*, 271:108171, 2 2022.

[29] Roseanna N Zia, Benjamin J Landrum, and William B Russel. A micro-mechanical study of coarsening and rheology of colloidal gels: Cage building, cage hopping, and smoluchowski's ratchet. *Journal of Rheology*, 58:1121, 2014.

[30] Jan Spitzer and Bert Poolman. The role of biomacromolecular crowding, ionic strength, and physicochemical gradients in the complexities of life's emergence. *Microbiology and Molecular Biology Reviews*, 73:371–388, 2009.

[31] Rico F Tabor, Chu Wu, Franz Grieser, Raymond R Dagastine, and Derek Y C Chan. Measurement of the hydrophobic force in a soft matter system. *J. Phys. Chem. Lett*, 4:3877, 2013.

[32] Benjamin Folch, Marianne Rooman, and Yves Dehouck. Thermostability of salt bridges versus hydrophobic interactions in proteins probed by statistical potentials. *J. Chem. Inf. Model.*, 48:119–127, 2008.

[33] D. Eric Anderson, Wayne J. Becktel, and F. W. Dahlquist. ph-induced denaturation of proteins: A single salt bridge contributes 3-5 kcal/mol to the free energy of folding of t4 lysozyme. *Biochemistry*, 29:2403–2408, 3 1990.

[34] Liguo Jiang, Siqin Cao, Peter Pak Hang Cheung, Xiaoyan Zheng, Chris Wai Tung Leung, Qian Peng, Zhigang Shuai, Ben Zhong Tang, Shuhuai Yao, and Xuhui Huang. Real-time monitoring of hydrophobic aggregation reveals a critical role of cooperativity in hydrophobic effect. *Nature Communications 2017 8:1*, 8:1–8, 5 2017.

[35] Marie Leijonmarck and Anders Liljas. Structure of the c-terminal domain of the ribosomal protein l7l12 from escherichia coli at 1.7 å. *Journal of Molecular Biology*, 195:555–579, 6 1987.

[36] Jennifer L. Hofmann, Akshay J. Maheshwari, Alp M. Sunol, Drew Endy, and Roseanna N. Zia. Ultra-weak protein-protein interactions can modulate proteome-wide searching and binding. *bioRxiv*, page 2022.09.30.510365, 10 2022.

[37] Lilian C. Johnson, Roseanna N. Zia, Esmaeel Moghimi, and George Petekidis. Influence of structure on the linear response rheology of colloidal gels. *Journal of Rheology*, 63:583, 5 2019.
[38] Eric F. Pettersen, Thomas D. Goddard, Conrad C. Huang, Elaine C. Meng, Gregory S. Couch, Tristan I. Croll, John H. Morris, and Thomas E. Ferrin. Ucsf chimerax: Structure visualization for researchers, educators, and developers. *Protein Science*, 30:70–82, 1 2021.
[39] Paul Langevin. Sur la theorie du mouvement brownien. *Comptes-rendus de l'Académie des sciences*, 146:530–533, 1908.
[40] L. Martinez, R. Andrade, E. G. Birgin, and J. M. Martínez. PACKMOL: A package for building initial configurations for molecular dynamics simulations. *J. Comput. Chem.*, 30(13):2157–2164, oct 2009.
[41] Michael P. Allen and Dominic J. Tildesley. *Computer Simulation of Liquids*. Oxford University Press, 2nd editio edition, 11 2017.
[42] Axel Brünger, Charles L. Brooks, and Martin Karplus. Stochastic boundary conditions for molecular dynamics simulations of st2 water. *Chemical Physics Letters*, 105:495–500, 3 1984.
[43] William Humphrey, Andrew Dalke, and Klaus Schulten. Vmd: Visual molecular dynamics. *Journal of Molecular Graphics*, 14:33–38, 2 1996.
[44] C.W.J Beenakker and P. Mazur. Diffusion of spheres in a concentrated suspension ii. *Physica*, 126A, 1984.
[45] John F. Brady. The long-time self-diffusivity in concentrated colloidal dispersions. *Journal of Fluid Mechanics*, 272:109–134, 1994.
[46] George Gabriel Stokes. On the effect of the internal friction of fluids on the motion of pendulums. *Transactions of the Cambridge Philosophical Society*, 9, 1851.
[47] A. Einstein. Über die von der molekularkinetischen theorie der wärme geforderte bewegung von in ruhenden flüssigkeiten suspendierten teilchen. *Annalen der Physik*, 322:549–560, 1 1905.
[48] Roseanna N Zia. Active and Passive Microrheology: Theory and Simulation. *Annu. Rev. Fluid Mech*, 50:371–405, 2018.
[49] Donald A McQuarrie. *Statistical mechanics*. Harper & Row, New York, 1976.
[50] Joshua S. Madin, Daniel A. Nielsen, Maria Brbic, Ross Corkrey, David Danko, Kyle Edwards, Martin K.M. Engqvist, Noah Fierer, Jemma L. Geoghegan, Michael Gillings, Nikos C. Kyrpides, Elena Litchman, Christopher E. Mason, Lisa Moore, Søren L. Nielsen, Ian T. Paulsen, Nathan D. Price, T. B.K. Reddy, Matthew A. Richards, Eduardo P.C. Rocha, Thomas M. Schmidt, Heba Shaaban, Maulik Shukla, Fran Supek, Sasha G. Tetu, Sara Vieira-Silva, Alice R. Wattam, David A. Westfall, and Mark Westoby. A synthesis of bacterial and archaeal phenotypic trait data. *Sci. Data 2020 71*, 7(1):1–8, jun 2020.
[51] Jerome K. Percus and George J. Yevick. Analysis of Classical Statistical Mechanics by Means of Collective Coordinates. *Phys. Rev.*, 110(1):1, apr 1958.
[52] W R Smith, D J Henderson, P J Leonard, J A Barker, and E W Grundke. Fortran codes for the correlation functions of hard sphere fluids. *Mol. Phys.*, 106(1):3–7, 2008.
[53] Loup Verlet and Jean Jacques Weis. Equilibrium Theory of Simple Liquids. *Phys. Rev. A*, 5(2):939, feb 1972.
[54] E. W. Grundke and D. Henderson. Distribution functions of multi-component fluid mixtures of hard spheres. *Mol. Phys.*, 24(2):269–281, aug 2006.
[55] Hans Bisswanger. Multiple Equilibria, Principles, and Derivations. In *Enzym. Kinet.*, pages 1–26. John Wiley & Sons, Ltd, jun 2017.
[56] B W Clare and D L Kepert. The closest packing of equal circles on a sphere. *Proc. R. Soc. London. A. Math. Phys. Sci.*, 405(1829):329–344, jun 1986.
[57] Jean Pierre Hansen and Ian R. McDonald. *Theory of simple liquids*. Elsevier Academic Press, 3rd ed. edition, 2006.
[58] Alice L. Thorneywork, Roland Roth, Dirk G.A.L. Aarts, and Roel P.A. Dullens. Communication: Radial distribution functions in a two-dimensional binary colloidal hard sphere system. *The Journal of Chemical Physics*, 140:161106, 4 2014.

SI APPENDIX

Supplementary methods

Rescaling of diffusivity: confinement and hydrodynamics

To compare the long-time self-diffusivities D^s_∞ calculated in our simulations to those from *in vivo* particle tracking experiments [18], we derived a volume fraction dependent scaling factor to account for the effects of hydrodynamic interactions (HI) and confinement. The long-time self-diffusivity, D^s_∞, of a suspension of purely-repulsive hard spheres can be expressed [45] as:

$$D^s_\infty = D^s_0 \left[1 + 2\phi g(2,\phi)\right]^{-1}, \tag{S1}$$

where D^s_0 is the short-time self-diffusivity, ϕ is the volume fraction, and $g(2,\phi)$ is the value of the radial distribution function at contact for a given volume fraction ϕ. Our simulations represent the unbound freely-draining limit in which D^s_0 is simply D_0, the Stokes-Einstein equation of a single colloid diffusing in a continuum liquid [46, 47]. Thus,

$$\left.\frac{D^s_\infty}{D_0}\right|_{\text{unb}} = \left[1 + 2\phi g(2,\phi)\right]^{-1}, \tag{S2}$$

holds in the unbound, freely-draining limit (solid black line, **Fig. S12A**). The analytical form of D^s_0 calculated by Beenakker and Mazur in 1984 [44] gives:

$$\left.\frac{D^s_\infty}{D_0}\right|_{\text{unb,HI}} = \left(1 - 1.73\phi + 0.88\phi^2\right)\left[1 + 2\phi g(2,\phi)\right]^{-1}, \tag{S3}$$

for the unbound case with full HI (solid red line, **Fig. S12A**). Analogous analytical forms of D^s_0 do not yet exist for confined suspensions, so we turned to results from dynamic simulations. The confined D^s_0 are calculated from confined Brownian (dashed black line, **Fig. S12A**; freely-draining limit [22]) and Stokesian Dynamics simulations (dashed red line, **Fig. S12A**; with HI [20]), averaged over all positions in a spherical cavity with a confinement ratio of $\lambda_\text{c} = a_\text{p}/a_\text{cav}$, where a_p and a_cav are the radii of the particle and cavity, respectively. In all cases, $g(2,\phi)$ was calculated via Percus-Yevick theory, as described in the subsequent section.

The volume fraction dependent scaling factor, s, is determined by the ratio of D^s_∞/D_0 for the unbound case and confined case with HI. The scaling factor increases with volume fraction (**Fig. S12A**), as crowding compounds the slow-down in diffusion from both hydrodynamic interactions and confinement. All instances of D^s_∞ in our work are divided by the value of $s(\phi)$, fit to a second-order polynomial in Python (**Fig. S12B**).

Theory for the bidisperse radial distribution function

We computed the radial distribution function $g(r)$ in translation voxels without small cytoplasmic proteins using Percus-Yevick (PY) theory [51]. We calculated $g(r)$ for bidisperse voxels using the code provided in [52] to numerically evaluate PY theory for hard sphere mixtures [53, 54] representing the size and abundance of ternary complexes and ribosomes across *E. coli* growth rates (Table S1). We examined two cases. First, we computed $g(r)$ when the total voxel volume V_tot is the same as in the tridisperse case, i.e., if crowders are simply removed (solid line, **Fig. S14B**). Second, we computed $g(r)$ when the total volume fraction ϕ_tot matches the tridisperse case, i.e., if crowders are removed and the voxel volume is reduced to recover the lost particle density (dashed line, **Fig. S14B**). To estimate the strength of this apparent depletion interaction, we ran dynamic simulations of bidisperse voxels across all *E. coli* growth rates, with volumes V_tot matching the tridisperse case. We included a $\varepsilon_\text{t,r} = 1\,k_\text{B}T$ attraction between ternary complexes and ribosomes (of the form in Eq. 1 and calculated $g(r)$ as described above via Eq. S5.

Binding affinity

We calculated the apparent binding affinity of the interaction between ribosomes and ternary complexes, as defined in [55]:

$$K_\text{d,app} = n\,[R]_\text{tot}\,\frac{[T]_\text{free}}{[T]_\text{bound}} - [T]_\text{free}, \tag{S4}$$

x where we assume each ribosome has n independent sites to which ternary complexes can bind. $[R]_\text{tot}$ is the total concentration of ribosomes, and $[T]_\text{free}$ and $[T]_\text{bound}$ are the concentrations of free and bound ternary complexes, respectively. Ribosome-bound ternary complexes are defined as in Eq. 8, i.e., if they are found within r_cut of a ribosome. For the case with isotropic attractions, the number of independent binding sites n is set by the number of ternary complexes that can fit around a ribosome at maximum packing. With a relative particle size ratio of $a_\text{tern}/a_\text{rib} = 0.45$, the isotropic number of binding sites is thus $n_\text{iso} = 32$ [56]. For the limited-valency attraction case, we set the number of binding sites $n_\text{lim} = 5$ to reflect the maximum measured coordination number of ribosomes, N_c (see **Fig. S2**, **Fig. S16B**, **Fig. S17B**)

Suspension Microstructure

We calculated the radial distribution function, $g(r)$, to characterize pair-level correlations between ternary complexes and ribosomes, defined according to [57, 58]

$$g(r) = \frac{V_\text{tot}}{N_\text{rib}N_\text{tern}}\left\langle \sum_{i=1}^{N_\text{rib}}\sum_{j=1}^{N_\text{tern}} \delta\left(\boldsymbol{r} + \boldsymbol{r}_i - \boldsymbol{r}_j\right)\right\rangle, \tag{S5}$$

where $V_\text{tot} = (l_\text{vox})^3$ is the total voxel volume and the function $\sum_{i=1}^{N_\text{rib}}\sum_{j=1}^{N_\text{tern}}\delta\left(\boldsymbol{r} + \boldsymbol{r}_i - \boldsymbol{r}_j\right)$ is the microscopic particle density at a given position $\boldsymbol{r}$, calculated in translation voxels with separations $\boldsymbol{r}_i - \boldsymbol{r}_j$ for all i ribosome and j ternary complex pairs. The radial distribution function is normalized to reflect departures from a uniform distribution, $g(r) = 1$ that arise from finite size and other effects. Please see **Fig. S17A**.

We calculated the static structure factor $S(\boldsymbol{q})$, the wave-space equivalent of $g(r)$ that is typically obtained in scattering experiments [37, 57] according to:

$$S(\boldsymbol{q}) = \frac{1}{N}\sum_{k=1}^{N}\sum_{l=1}^{N} e^{-i\boldsymbol{q}\cdot(\boldsymbol{r}_k - \boldsymbol{r}_l)}, \tag{S6}$$

where $\boldsymbol{q}$ is the wavevector normalized by the ribosome size a_rib, N is the number of particles, and $\boldsymbol{r}_k - \boldsymbol{r}_l$ is the separation for a particle pair (k,l). $S(\boldsymbol{q})$ is radially averaged to give $S(q)$, where $q = |\boldsymbol{q}|$ and corresponds to a real space length of $l = 2\pi/q$. We are interested in quantifying long-range correlations throughout the translation voxel and thus calculated $S(q)$ for all particles $N = N_\text{rib} + N_\text{tern} + N_\text{prot}$ in the ensemble.

Coordination numbers

A ternary complex, i, is considered 'coordinated' with or bound to a ribosome, j, if their center-to-center separation r_{ij} is less than the maximum bond distance $r_{\mathrm{cut}} = 21$ nm. This value corresponds to a separation of 2.1 nm beyond hard-sphere contact, which includes the radii of the binding site protrusions and the width of the attractive well. According to this definition, we calculated the number of ternary complexes to which each ribosome is bound – its coordination number, N_{c}. We computed the distribution of ribosome coordination numbers for voxels across all growth rates and attraction strengths (**Fig. S3, S2**). We quantified the duration of individual binding events by computing the time that ternary complexes spend within the maximum bond distance r_{cut} of a ribosome (**Fig. S8A**).

Extrapolation of *in vivo* co-localization to faster growth rates

The fraction of ribosome-bound ternary complexes, f, has been measured *in vivo* at only one growth rate, $f^{\mathrm{exp}}(1\,\mathrm{dbl/hr}) = 0.6$. We extrapolated this *in vivo* measurement to faster cellular growth rates (**Fig. S1**) by calculating the expected change due to crowding ($+\Delta f_{\mathrm{crowd}}$) and stoichiometry ($+\Delta f_{\mathrm{stoich}}$). We defined the change in co-localization due to purely entropic forces as:

$$\Delta f_{\mathrm{crowd}}(\mathrm{gr}) = f^{\mathrm{iso,HS}}(\mathrm{gr}) - f^{\mathrm{iso,HS}}(1\,\mathrm{dbl/hr}) \tag{S7}$$

or the change in f with growth rate in the baseline hard sphere simulations (Fig. 4A, $\varepsilon_{\mathrm{t,r}} = 0\,k_{\mathrm{B}}T$. We define the change in co-localization due to stoichiometry as:

$$\Delta f_{\mathrm{stoich}}(\mathrm{gr}) = f^{\mathrm{max}}(\mathrm{gr}) - f^{\mathrm{max}}(1\,\mathrm{dbl/hr}) \tag{S8}$$

where $f^{\mathrm{max}}(\mathrm{gr}) = 4N_{\mathrm{rib}}(\mathrm{gr})/N_{\mathrm{tern}}(\mathrm{gr})$ is the maximum possible f, assuming that each ribosome is bound to exactly four ternary complexes. $N_{\mathrm{rib}}(\mathrm{gr})$ and $N_{\mathrm{tern}}(\mathrm{gr})$ were extracted and compiled from whole-cell measurements by [3]. We summed these two contributions ($+\Delta f_{\mathrm{tot}}$) to obtain the extrapolated *in vivo* bound fraction:

$$f^{\mathrm{exp}}(\mathrm{gr}) = f^{\mathrm{exp}}(1\,\mathrm{dbl/hr}) + \Delta f_{\mathrm{tot}}(\mathrm{gr}) \tag{S9}$$

Supplementary results

Static structure factor

We calculated the static structure factor, $S(q)$, in translation voxels across all *E. coli* growth rates and isotropic attraction strengths studied in this work (**Fig. S5**). In the hard sphere limit ($\varepsilon_{\mathrm{t,r}} = 0\,k_{\mathrm{B}}T$), we found that cytoplasmic polydispersity prevents the emergence of strong structural correlations at any wavevector q or real space length $l = 2\pi/q$. The probability of long-range correlations at small wavevectors is only slightly increased by weak isotropic attractions ($\varepsilon_{\mathrm{t,r}} = 3\,k_{\mathrm{B}}T$), suggesting the formation of transient low-order clusters. A single peak emerges for the $\varepsilon_{\mathrm{t,r}} = 6\,k_{\mathrm{B}}T$ attractive case, characteristic of a bicontinuous gel created by arrested phase separation. The peak shifts to higher wavevectors as crowding increases, corresponding with formation of thinner and shorter strands. In the $\varepsilon_{\mathrm{t,r}} = 16\,k_{\mathrm{B}}T$ attractive case, there is an abundance of correlations at longer length-scales (shorter wavevectors), but the stringier structure is not as well characterized by a single length-scale since ongoing phase separation is slowed by strong bonding [37].

Effective cytoplasmic viscosity

We calculated the effective cytoplasmic viscosity experienced by ternary complexes as a function of cellular growth rate, accounting for the impacts of hydrodynamic interactions and cellular confinement (see ***Methods*** above). Without attractions ($\varepsilon_{\mathrm{t,r}} = 0\,k_{\mathrm{B}}T$), the effective viscosity exhibits the expected increase with volume fraction, but underpredicts by two- to three-fold the *in vivo* estimate for equivalently-sized proteins in *E. coli* [18] (**Fig. S15, Fig. ??**). Transient cluster formation in the case of weak isotropic attractions ($\varepsilon_{\mathrm{t,r}} = 3\,k_{\mathrm{B}}T$) drives an approximately 5% increase in effective viscosity, whereas stronger isotropic attractions over-predict *in vivo* viscosity by up to five-fold ($\varepsilon_{\mathrm{t,r}} = 6\,k_{\mathrm{B}}T$) and up to two orders of magnitude ($\varepsilon_{\mathrm{t,r}} = 16\,k_{\mathrm{B}}T$). In all cases, viscosity increases with cell growth rate as the cytoplasm densifies.

Supplementary tables

Table S1: Growth-rate dependent simulation parameters in translation voxels of *E. coli* cytoplasm

Doublings/hr	$\mu = 1.0$	$\mu = 1.5$	$\mu = 2.0$	$\mu = 2.5$	$\mu = 3.0$
N_{rib}	659	1,005	1,266	1,426	1,524
N_{tern}	3,528	4,662	6,090	7,476	8,820
N_{prot}	176,064	198,801	205,610	194,020	172,200
l_{vox}	405.0 nm	404.4 nm	403.7 nm	404.3 nm	404.0 nm
ϕ_{tot}	0.224	0.299	0.359	0.392	0.413

Supplementary figures

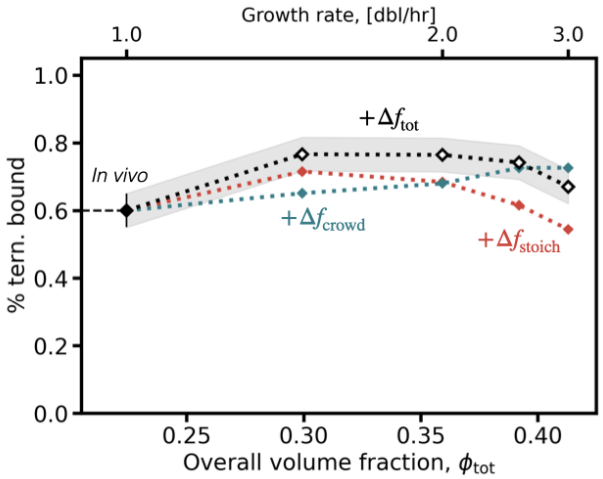

Figure S1: *In vivo* co-localization of ternary complexes and ribosomes is projected to increase non-monotonically as a function of growth rate. Extrapolation of the measured *in vivo* fraction of ribosome-bound ternary complexes, f, at 1 dbl/hour (black solid diamond) to higher growth rates (see Supplementary Methods). The change in co-localization due to entropic forces ($+\Delta f_{\mathrm{crowd}}$, teal) and changing relative stoichiometry ($+\Delta f_{\mathrm{stoich}}$, orange), assuming each L7/L12 is bound to one ternary complex. These two contributions are summed to obtain the extrapolated *in vivo* prediction to higher growth rates ($+\Delta f_{\mathrm{tot}}$, black), including errors carried forward from the experimental measurement at 1 dbl/hour.

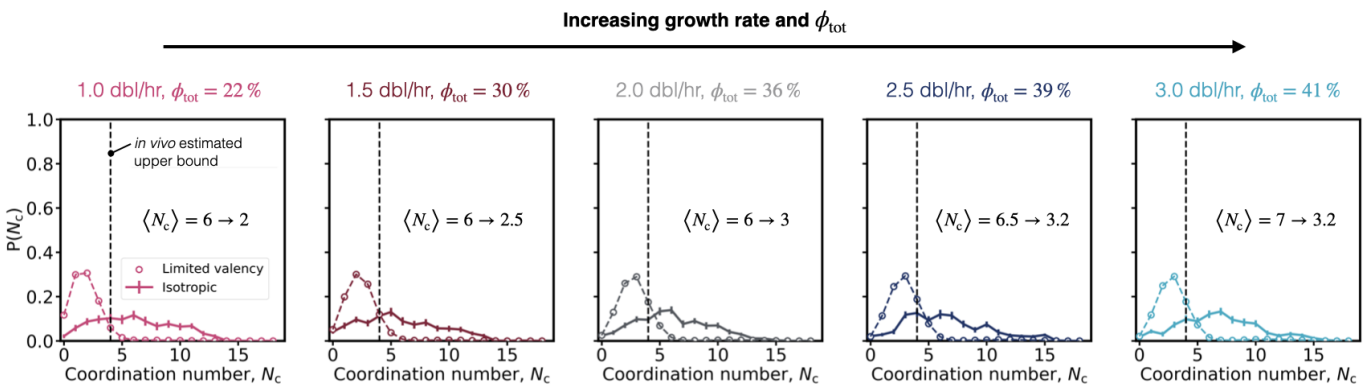

Figure S2: Limited valency attractions drive biofidelic co-localization of translation molecules, without higher-order microstructure. Coordination number distributions highlight an increase in the number of ternary complexes bound to each ribosome, both with increasing growth rate (red to grey to blue) and interaction valency (dashed versus solid lines) for attractions of strength $\varepsilon_{t,r} = 16\,k_B T$. The estimated maximum ribosome occupancy from experiments [9] is four ternary complexes per ribosome, marked by a vertical dashed line. A reduction in the average number of ternary complex contacts, $\langle N_c \rangle$, felt by ribosomes is noted for the isotropic case relative to the limited valency case, at each growth rate (left to right).

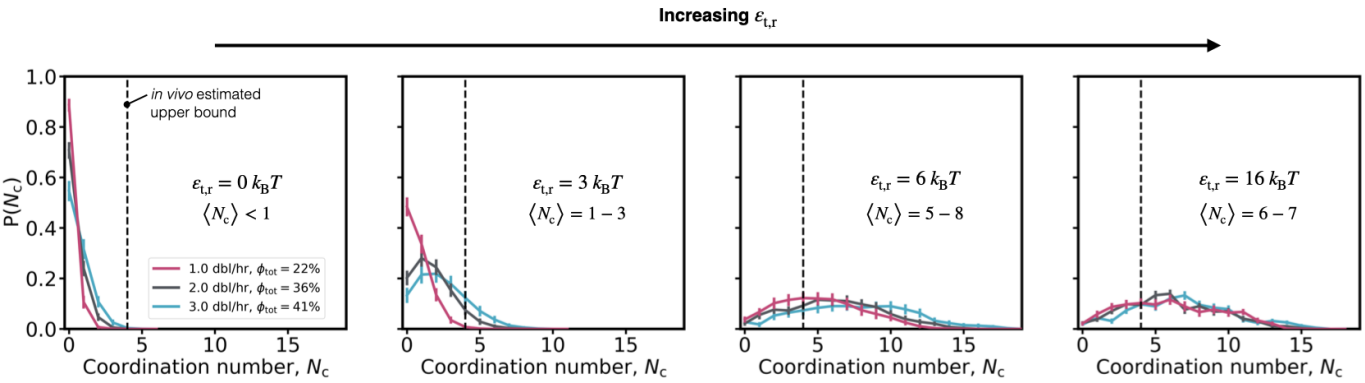

Figure S3: Strong isotropic $\varepsilon_{t,r} \approx 6 - 16\,k_B T$ attractions drive unphysiological coordination numbers of ternary complexes around ribosomes. Coordination number distributions highlight an increase in the number of ternary complexes bound to each ribosome, both with increasing growth rate (red to grey to blue) and attraction strength (left to right). The average number of ternary complex contacts per ribosome, $\langle N_c \rangle$, exceeds the *in vivo* estimate of 4 ternary complexes per ribosome (vertical dashed black line, [9]) for attraction strengths $\varepsilon_{t,r} > 6\,k_B T$. In our model, isotropic attraction allows a maximum of $N_c = 32$ based on close packing of spheres of size $a_{tern} = 5.9\,\mathrm{nm}$ around spheres of size $a_{rib} = 13\,\mathrm{nm}$ [56].

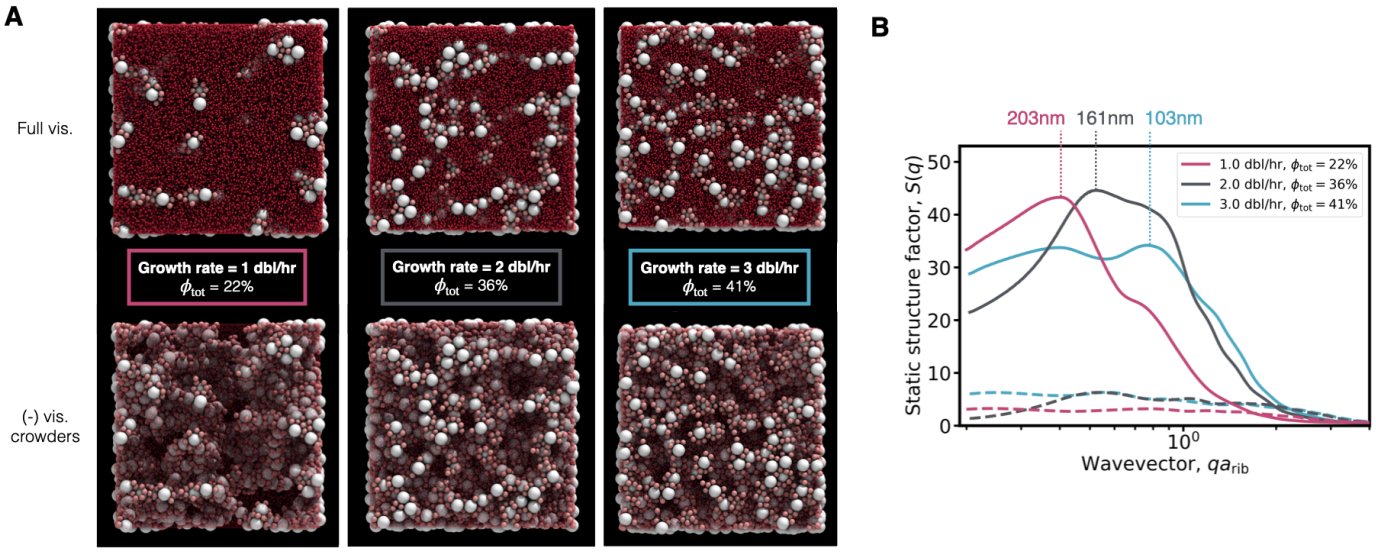

Figure S4: Schematics for modeling physical interactions and chemical reactions in translation voxels of the E. coli cytoplasm in LAMMPS. (A) Visualizations of E. coli translation voxels with strong isotropic attractions ($\varepsilon_{\mathrm{t,r}}^{\mathrm{exp}} = 16\,k_{\mathrm{B}}T$) between ternary complexes and ribosomes at three growth rates (left to right). ϕ is the total system volume fraction (see ***Methods***), which increases from 22% to 41% as cell growth rate increases. **(Upper)** Full visualization with ribosomes (white), ternary complexes (pink), and crowder proteins (red). **(Lower)** Visualizations with transparent crowder proteins, highlighting the internal voxel microstructure. **(B)** Static structure factor, $S(q)$, for growth rates of 1 (magenta), 2 (grey), and 3 dbl/hr (cyan) for the hard sphere ($\varepsilon_{\mathrm{t,r}}^{\mathrm{exp}} = 0\,k_{\mathrm{B}}T$, dashed lines) and strongly attractive ($\varepsilon_{\mathrm{t,r}}^{\mathrm{exp}} = 16\,k_{\mathrm{B}}T$, solid lines) cases. The peak, corresponding to the most abundant suspension length scale in real space, is marked with vertical dotted lines. **(C)** Effective cytoplasmic viscosity, $\eta_{\mathrm{eff,tern}}$, experienced by ternary complexes in translation voxels (Eq. 7), versus growth rate and volume fraction for the hard sphere (blue) and strongly attractive (red) cases. The viscosity of water, η_0, at a temperature of 37C (horizontal dashed line) and the estimated *in vivo* viscosity experienced in *E. coli* by a protein with the same molecular weight as a ternary complex (horizontal dotted line [18]) are marked.

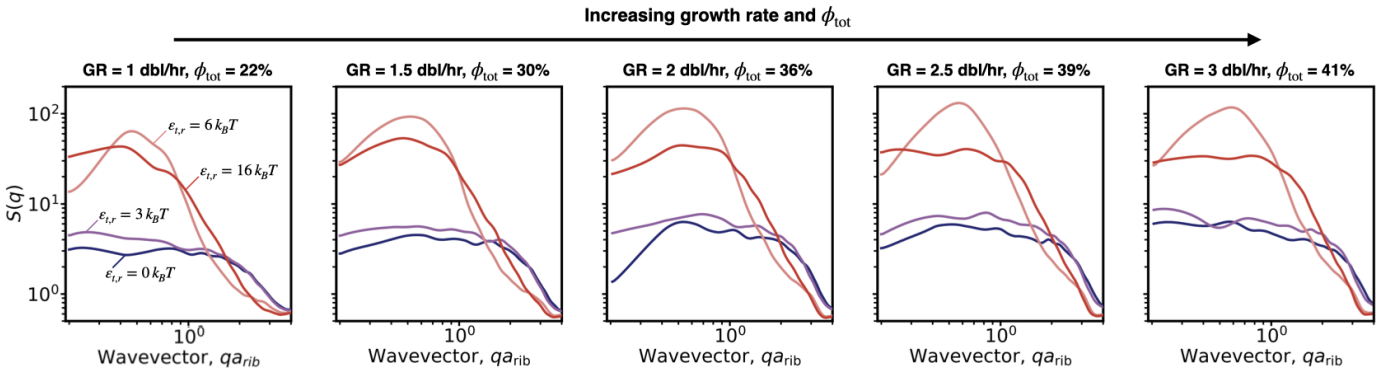

Figure S5: Structural length scales in the *E. coli* cytoplasm. Static structure factor, $S(q)$, as a function of cellular growth rate and overall volume fraction (left to right, marked at top), and strength of attractions between ternary complexes and ribosomes (colors, marked inset on left). The probability of long-range correlations at small wavevectors is only slightly increased by weak isotropic attractions ($\varepsilon_{\mathrm{t,r}} = 3\,k_{\mathrm{B}}T$), suggesting the formation of transient low-order clusters. A single peak emerges for the $\varepsilon_{\mathrm{t,r}} = 6\,k_{\mathrm{B}}T$ attractive case, characteristic of a bicontinuous gel created by arrested phase separation. In the $\varepsilon_{\mathrm{t,r}} = 16\,k_{\mathrm{B}}T$ attractive case, there is an abundance of correlations at longer length-scales (shorter wavevectors), but the stringier structure is not as well characterized by a single length-scale since ongoing phase separation is slowed by strong bonding [37].

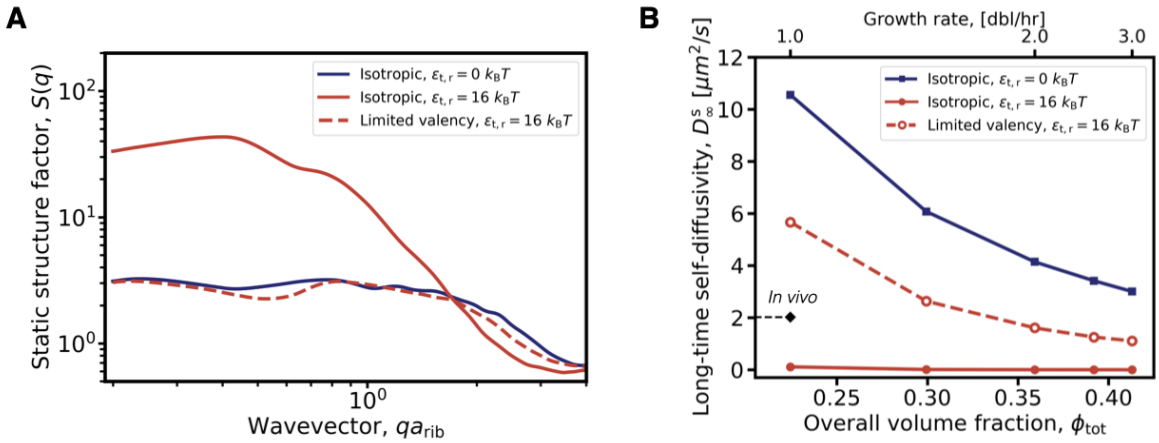

Figure S6: Limiting the valency of attractions between ternary complexes and ribosomes prevents arrested phase separation. (A). Static structure factor, $S(q)$, at a growth rate of 1 dbl/hr in the purely-repulsive limit (blue, solid line) and with isotropic (red, solid line) and limited valency (red, dashed line) attractions between ternary complexes and ribosomes. Limiting the interaction valency prevents the abundance of longer length-scale correlations observed in the isotropic case. **(B)**. Long-time self-diffusivity of ternary complexes as a function of growth rate and total volume fraction. The experimentally-observed apparent diffusivity is shown for a growth rate of 1.0 dbl/hr (♦) [9]. Limiting the interaction valency improves agreement with the in vivo measurement, without fully arresting dynamics as in the isotropic case. The remaining gap could be attributed to the limited temporal resolution of particle tracking experiments ($\sim 2\,\mathrm{ms}$), which are sufficiently large to sample the confinement in a given observation window. We thus might expect experimental measurements (♦) to be artificially low relative to our unbound simulations.

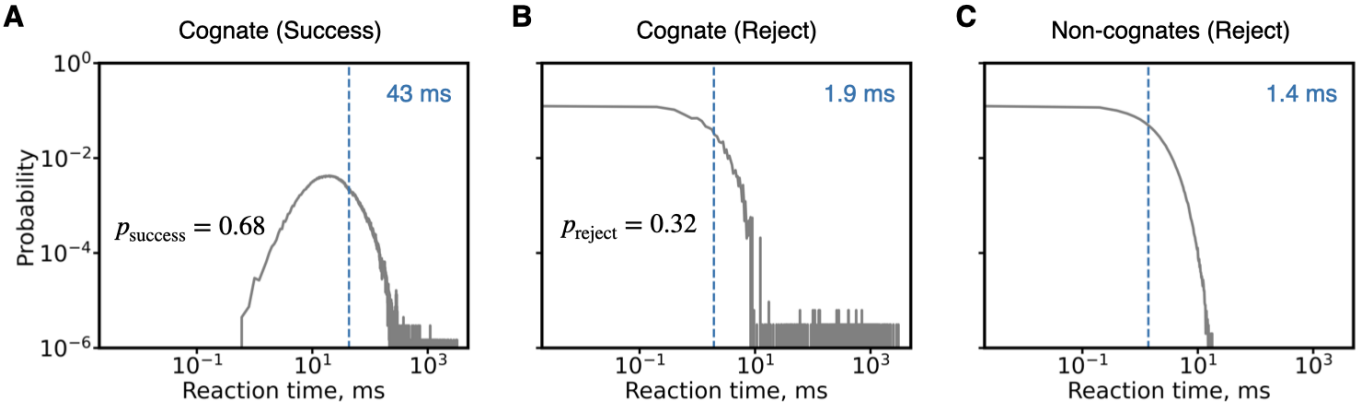

Figure S7: Distribution of time spent by cognate and non-cognate ternary complexes in reactions with ribosomes, computed by sampling kinetic trajectories. (A). Reaction times for cognate ternary complexes that successfully react (with probability p_{success} inset, black) and **(B)** those that are rejected (with probability p_{reject} inset, black). **(C)** Reaction times for non-cognate ternary complexes, of which all are rejected. In each plot, the average latency is marked (vertical blue dashed line, displayed at top right).

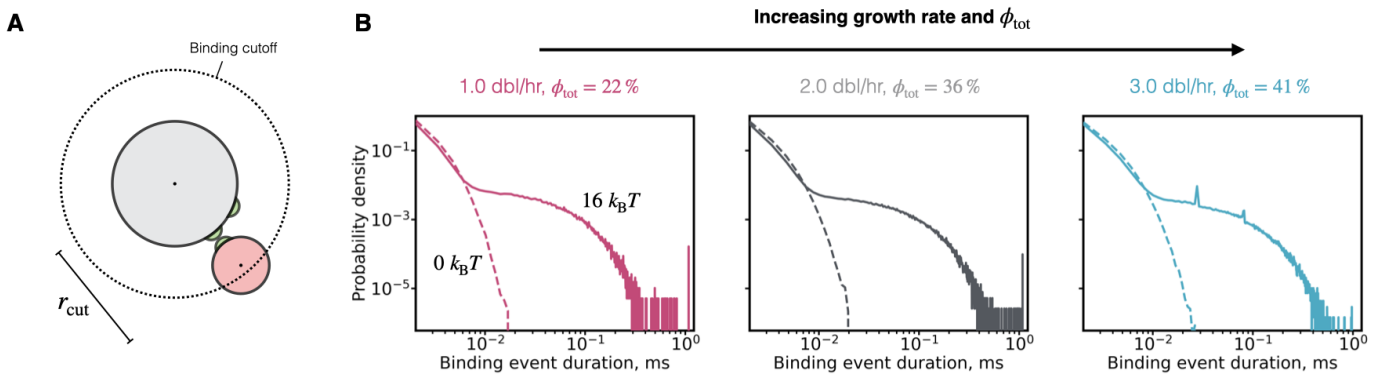

Figure S8: Probability distributions of the duration of physical ternary complex - ribosome binding events. (A). Schematic of binding cutoff between limited valence ternary complexes and ribosomes, chosen to be $r_{\mathrm{cut}} = 2.1\,\mathrm{nm}$ based on the radius of the binding site protrusions and width of the attractive potential well. **(B)**. Probability density function of the duration of binding events, defined as when a ternary complex and ribosome come within a bond distance (r_{cut}). Across all studied growth rates (left to right), purely entropic binding events are brief, lasting at most $\sim 20\ \mu\mathrm{s}$ (dashed lines, $0\,k_{\mathrm{B}}T$). The strong limited valence case (solid lines, $16\,k_{\mathrm{B}}T$) show binding times up to 1 ms, on the order of chemical reaction timescales, but below the upper limit of $2\,\mathrm{ms}$ inferred from experiment [9].

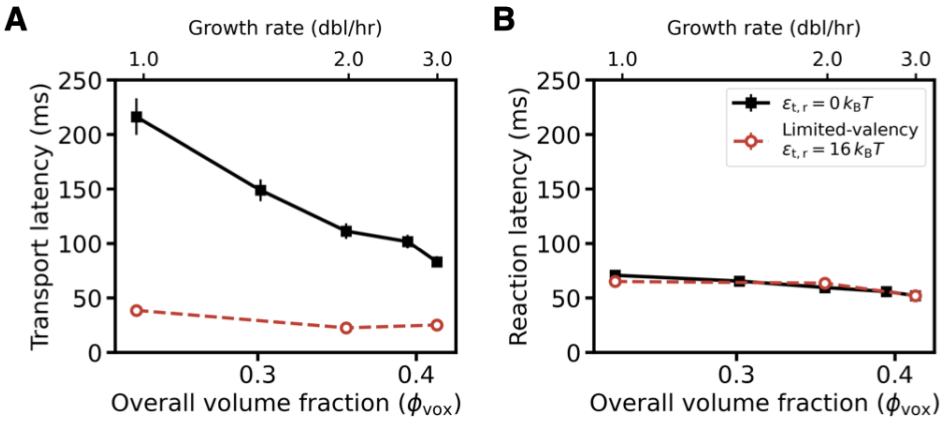

Figure S9: EF-Tu·L7/L12 interactions speed elongation by facilitating faster transport. Simulation results from translation voxels without attractions (black line, [3]) and with limited-valency attractions between ternary complexes and ribosomes (red line, this work). **(A)** Transport latency, which decreases with increasing growth rate (left to right), is reduced by pre-loading of ternary complexes onto ribosomes. **(B)** Reaction latency is unchanged by cognate-independent pre-loading.

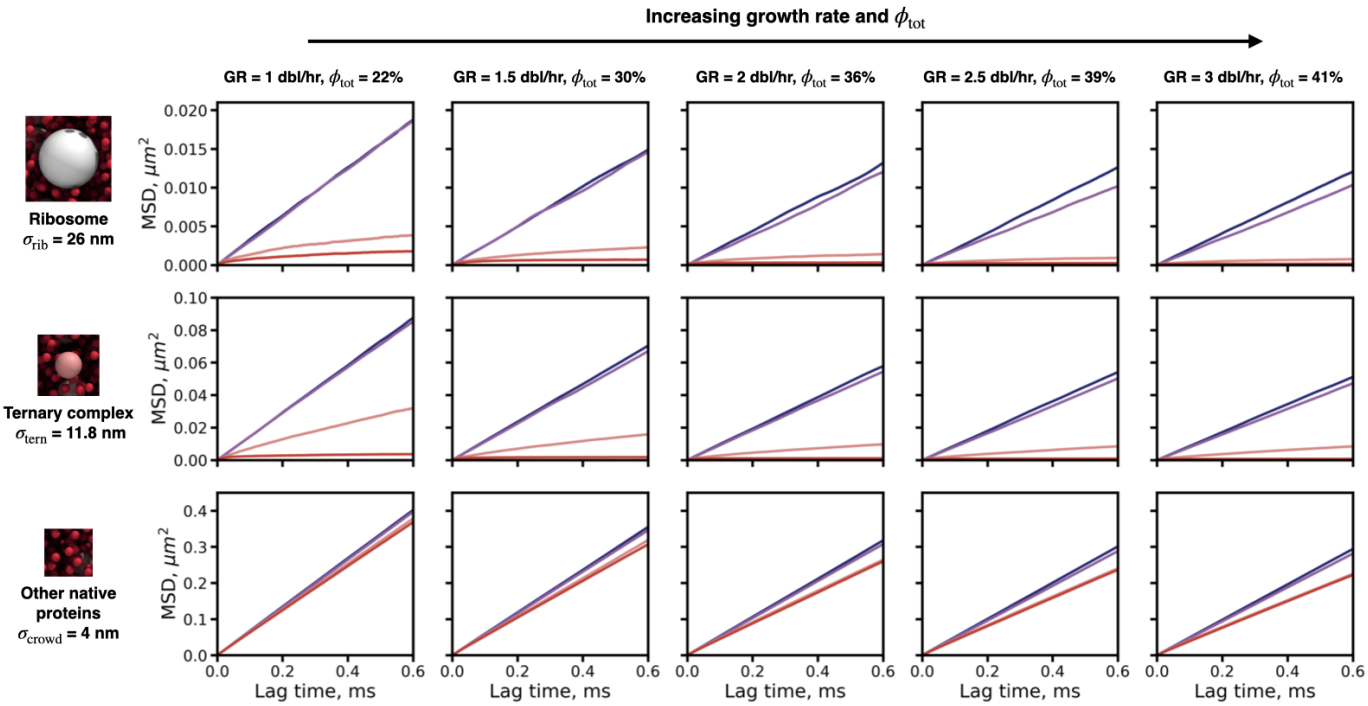

Figure S10: Dynamics of translation molecules are suppressed by increased crowding and attraction strength. Mean squared displacements versus lag time are plotted for ribosomes (top row), ternary complexes (middle row), and other native cytoplasmic proteins (bottom row), for each growth rate (left to right) and attraction strengths of $\varepsilon_{t,r} = 0\,k_B T$ (blue), $3\,k_B T$ (purple), $6\,k_B T$ (pink), and $16\,k_B T$ (red).

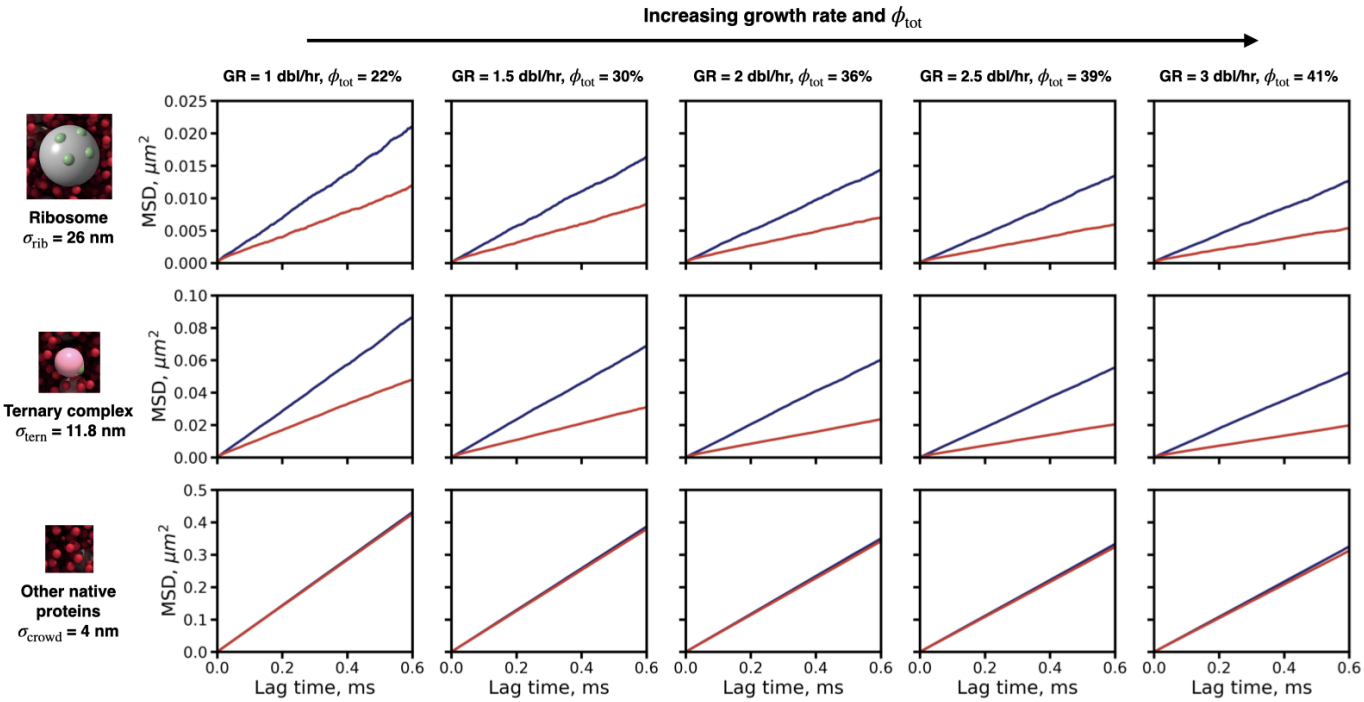

Figure S11: Limiting the valency of attractions between ternary complexes and ribosomes permits more particle mobility across growth rates. Mean squared displacements versus lag time are plotted for ribosomes (top row), ternary complexes (middle row), and other native cytoplasmic proteins (bottom row), for each growth rate (left to right) and limited valency attraction strengths of $\varepsilon_{\mathrm{t,r}} = 0\, k_{\mathrm{B}}T$ (blue) and $\varepsilon_{\mathrm{t,r}} = 16\, k_{\mathrm{B}}T$ (red).

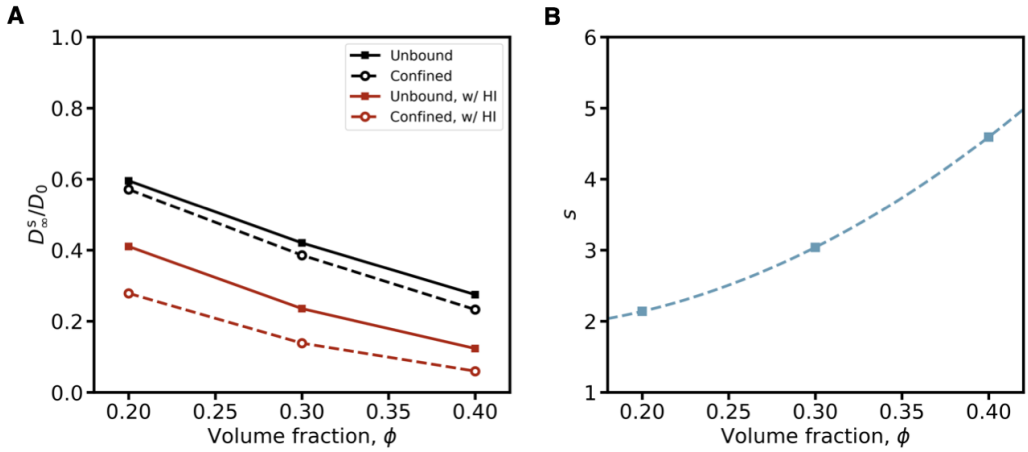

Figure S12: Hydrodynamic interactions and spherical confinement slow diffusion. (A) The long-time self-diffusivity, D^s_∞, normalized by the lone particle diffusivity, D_0, in a monodisperse hard sphere suspension, calculated as a function of volume fraction ϕ, the contact value of the radial distribution function g(r), and the short-time self-diffusivity D^s_0, as described in Supplementary Methods . The presence of both confinement (dashed lines) and hydrodynamic interactions (red lines) reduce the expected long-time self-diffusivity. **(B)** The scaling factor, s, is calculated via the ratio of D^s_∞ for the unbound and confined + HI cases (symbols), and is fit to a second-order polynomial across all volume fractions (dashed line).

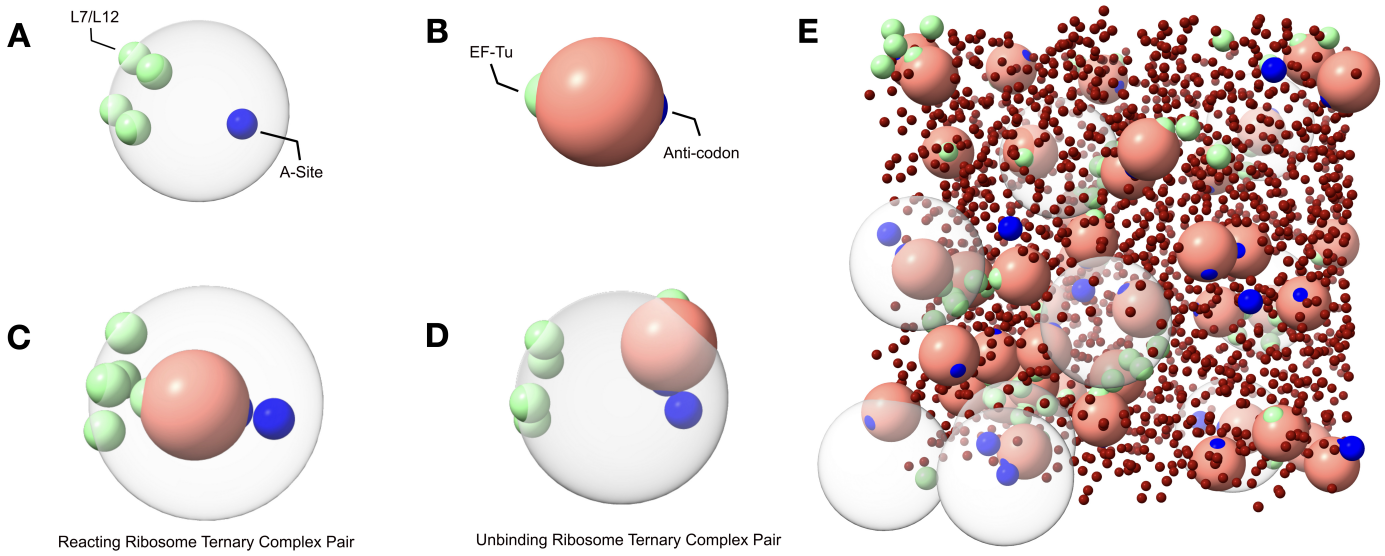

Figure S13: Schematics for modeling physical interactions and chemical reactions in translation voxels of the E. coli cytoplasm in LAMMPS. (A) Ribosomes (grey) are represented as rigid bodies with patches representing four L7/L12 subunits (green) and one internal A-site codon (blue). **(B)** Ternary complexes (pink) are represented with as rigid bodies with one EF-Tu (green) and anti-codon patch (blue). **(C)** After a reaction begins, the ternary complex is internalized within the ribosome by turning off the hard sphere repulsion and turning on a strong attraction between the A-site and anticodon. During reactions, other ternary complexes are allowed to occupy the three free L7/L12 subunits but are not allowed to enter the ribosome. **(D)** Following the conclusion of a reaction, the ternary complex is released by a soft Morse repulsion between formerly reacting pairs. **(E)** Thousands of unique translation voxels are simulated to capture the physiological distribution of translation molecules and to calculate reaction, transport, and elongation latencies. Visualizations were created using UCSF ChimeraX [38].

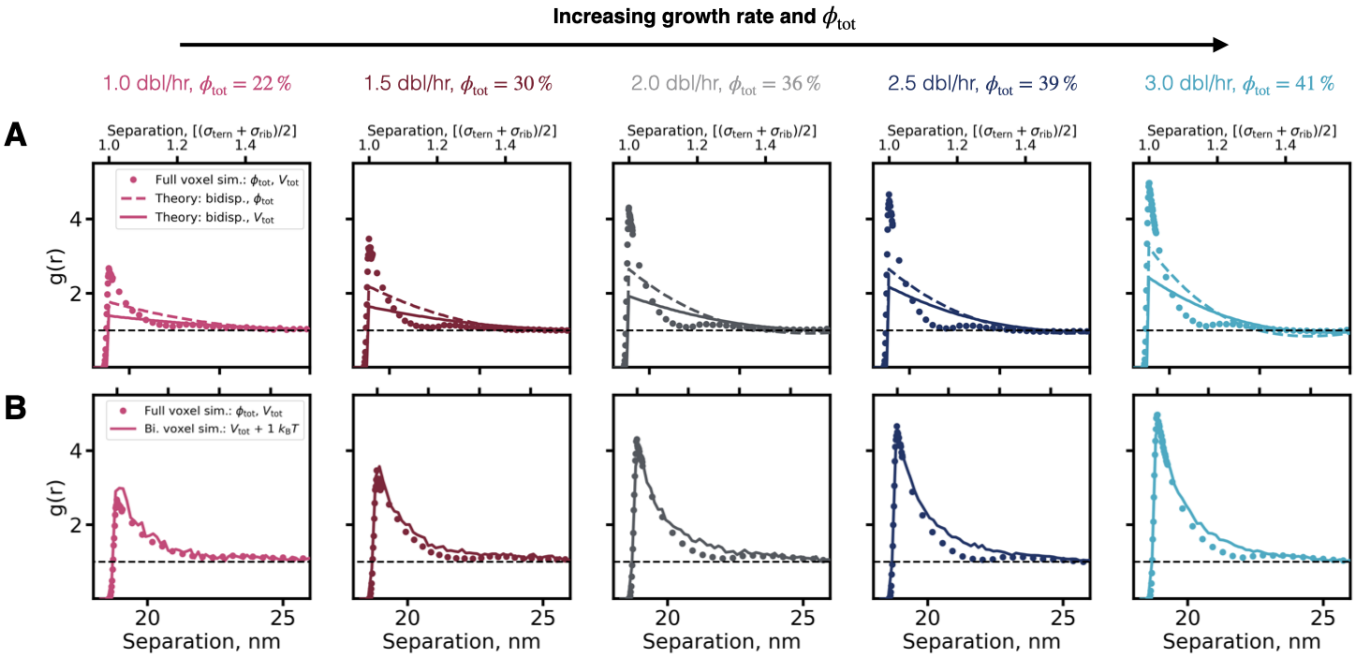

Figure S14: Small proteins in the *E. coli* cytoplasm induce depletion interactions of strength $\varepsilon_{t,r} \approx 1\,k_BT$ between translation molecules. (A). Radial distribution functions between ternary complexes and ribosomes, $g(r)$, calculated in simulations of translation voxels (symbols), highlight structural deviations from the ideal gas limit (dashed black line) across all growth rates. Analytical radial distribution functions, calculated for bidisperse suspensions of ternary complexes and ribosomes with the same abundances as in the full translation voxels, are also shown for systems with the same ϕ_{tot} (colored dashed line) and V_{tot} (colored solid line). Volume fraction alone is insufficient to recover the microstructure observed in full cytoplasmic voxels (i.e., the peak at contact, $18.9\,\mathrm{nm}$), suggesting the presence of depletion interactions. **(B)**. Bidisperse systems with added $\varepsilon_{t,r} = 1\,k_BT$ Yukawa attractions (solid lines) recover the contact peaks of the tridisperse $g(r)$, across all growth rates, thus estimating the strength of the depletion interaction.

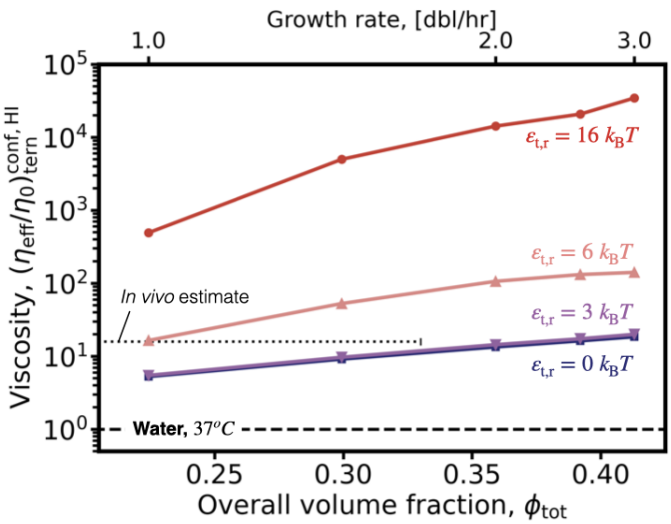

Figure S15: Arrest increases cytoplasmic viscosity beyond *in vivo* estimates. Effective cytoplasmic viscosity experienced by ternary complexes in translation voxels (Eq. **??**), versus growth rate and volume fraction for all studied attraction strengths of $\varepsilon_{\text{t,r}} = 0\,k_{\text{B}}T$ (blue), $3\,k_{\text{B}}T$ (purple), $6\,k_{\text{B}}T$ (pink), and $16\,k_{\text{B}}T$ (red). The viscosity of water, η_0, at a temperature of $37^o\,C$ (horizontal dashed line) and the estimated *in vivo* viscosity experienced by a protein with a molecular weight of 69 kDa (M_{tern}) in *E. coli* (horizontal dotted line, [18]) are marked.

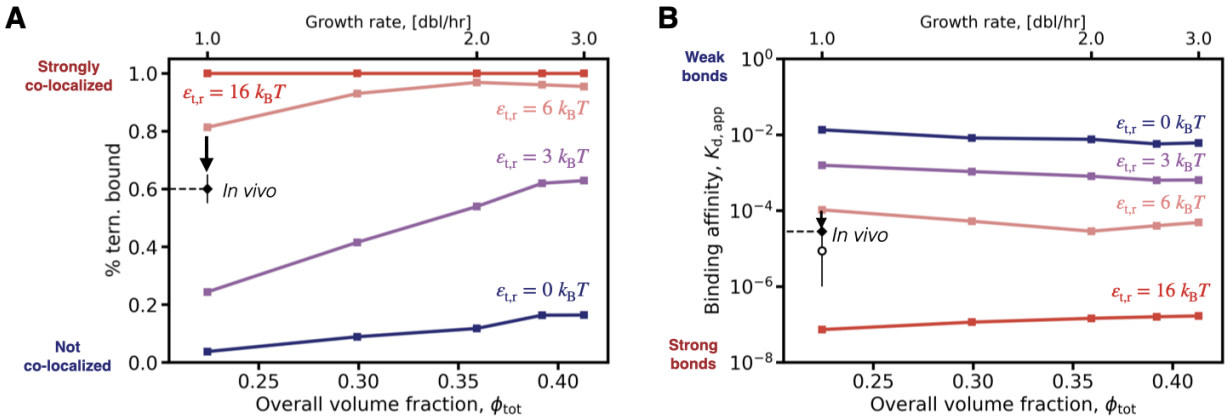

Figure S16: Physical co-localization and biochemical affinity measurements suggest that a limited interaction valency is needed to recover experimental measurements. (A) A measure of physical co-localization: the percent of ternary complexes bound to ribosomes for isotropic attraction strengths of $\epsilon_{t,r} = 0 - 16 k_b T$ (colors). Stronger attractions drive more co-localization of translation molecules, and suggest that an isotropic attraction strength less than $\epsilon_{t,r} = 6 k_b T$ would best recover experimental measurements at a growth rate of 1.0 dbl/hr (♦) [9]. **(B)** A measure of biochemical binding affinity: the apparent equilibrium dissociation constant $K_{d,app}$ for the interaction between ternary complexes and ribosomes, with isotropic attraction strengths of $\epsilon_{t,r} = 0 - 16 k_b T$ (colors). Stronger attractions drive stronger binding affinities, and suggest that an isotropic attraction strength greater than $\epsilon_{t,r} = 6 k_b T$ would best recover experimental measurements at a growth rate of 1.0 dbl/hr (♦) [9]. Validation of Eq. **??** is marked (o), assuming four binding sites on the ribosome, 60% of ternary complexes bound, and abundances and densities of the translation voxel at a growth rate of 1.0 dbl/hr.

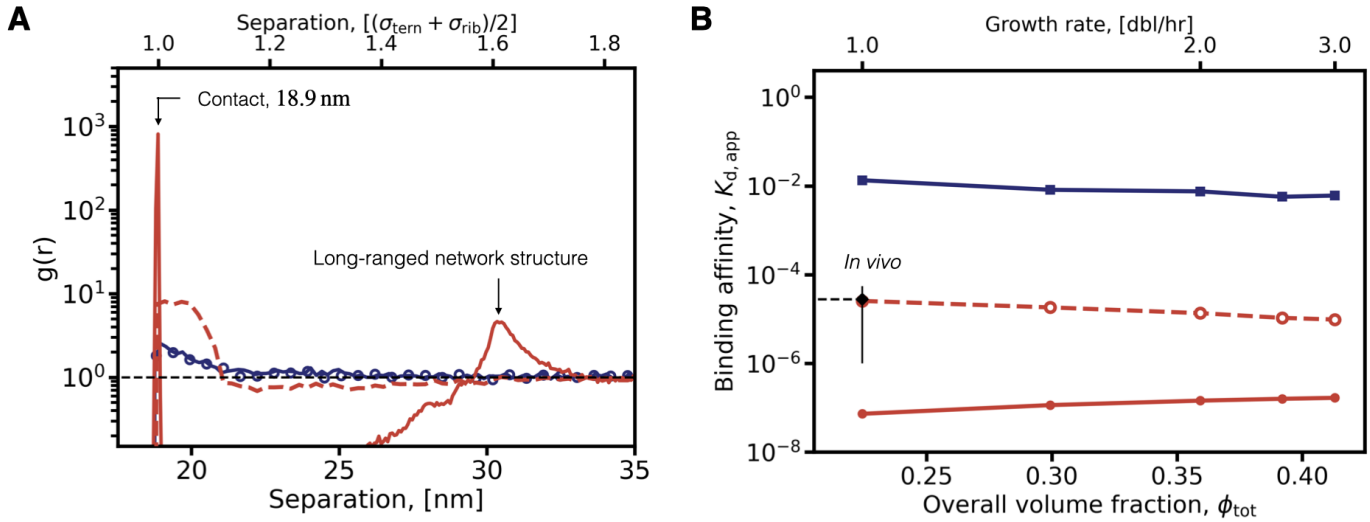

Figure S17: Limited-valency attractions between ternary complexes and ribosomes recover physiological levels of co-localization and binding affinity, while avoiding cytoplasmic arrest. (A) Radial distribution functions, $g(r)$, between ternary complexes and ribosomes at a growth rate of 1 dbl/hr and ϕ = 22%. The non-attractive limited-valency case (blue, symbols) quantitatively recovers the microstructure of the non-attractive isotropic case (blue, solid line). Strong isotropic attractions (red solid line) produce a high probability of finding a ternary complex and ribosome at contact, as well as a second peak corresponding with formation of long-ranged network structure. Strong limited-valency attractions (red dashed line) increase the contact peak versus the non-attractive case, while avoiding the second peak. **(B)** The apparent equilibrium dissociation constant $K_{\mathrm{d,app}}$ for the interaction between ternary complexes and ribosomes, as a function of growth rate.

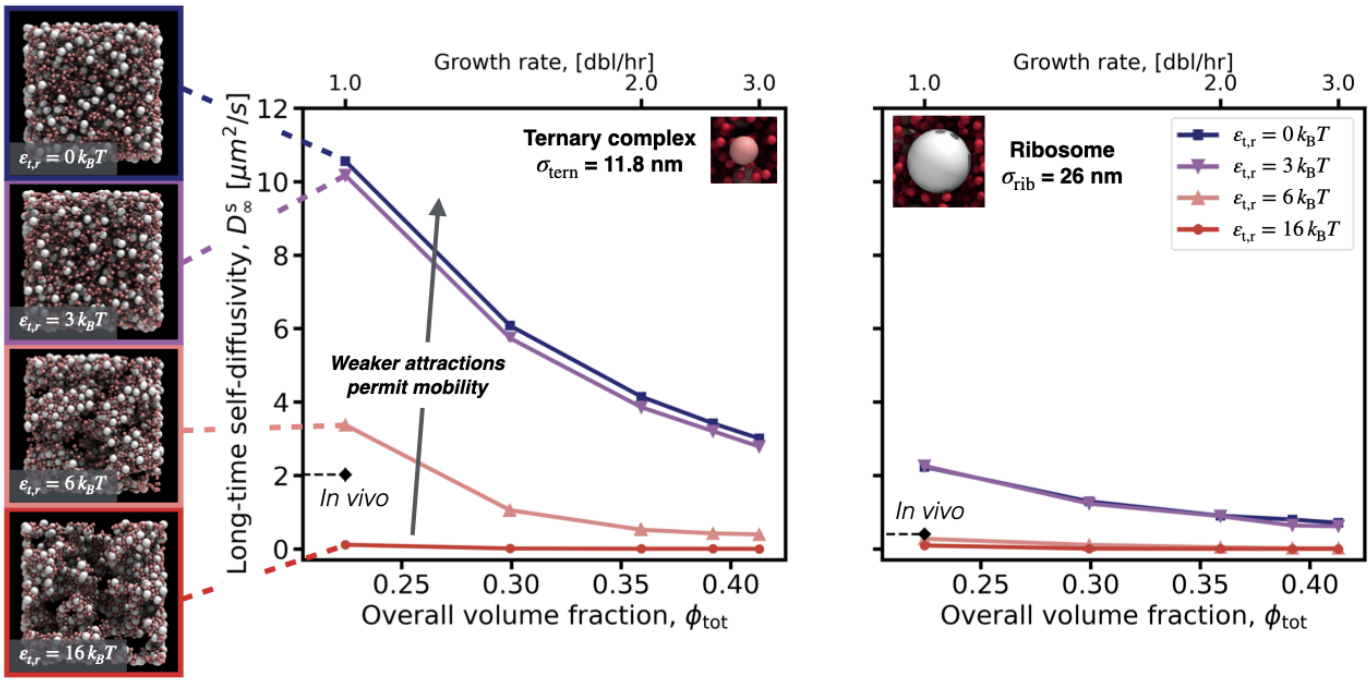

Figure S18: Isotropic attractions weak enough to avoid arrest permit faster diffusion than measured *in vivo*. The long-time self-diffusivity (Eq. 7) for ternary complexes (left) and ribosomes (right) as a function of growth rate and total volume fraction ϕ_{tot} , with isotropic attractions of strength $\varepsilon_{t,r} = 0 - 16\,k_BT$ (colors, inset legend). The experimentally-observed apparent diffusivity is shown for a growth rate of 1.0 dbl/hr (♦) for both ternary complexes and ribosomes [9]. Simulation screenshots of translation voxels at 1.0 dbl/hr at each studied attraction strength are shown (inset, left).